



www.sciencemag.org/cgi/content/full/science.aau7114/DC1

Supplementary Materials for

Volumetric additive manufacturing via tomographic reconstruction

Brett E. Kelly*, Indrasen Bhattacharya*, Hossein Heidari*, Maxim Shusteff, Christopher M. Spadaccini, Hayden K. Taylor†

*These authors contributed equally to this work.

†Corresponding author. Email: hkt@berkeley.edu

Published 31 January 2019 on *Science* First Release

DOI: 10.1126/science.aau7114

This PDF file includes:

- Materials and Methods
- Supplementary Text
- Figs. S1 to S20
- Tables S1 to S3
- Captions for Movies S1 to S5
- References

Other Supplementary Material for this manuscript includes the following:

(available at www.sciencemag.org/cgi/content/full/science.aau7114/DC1)

Movies S1 to S5 (.mov)

Materials and Methods

S1. Engineering polymers

The primary materials used for printing in this work were formulated from commercially-available acrylate photopolymers and photoinitiators. Sufficiently low values of absorption coefficient α are enabled by judicious selection of the photoinitiator molecule based on its molar absorptivity in the illuminating wavelength band and tuning of its concentration.

The material used in Fig. 1C–G and Fig. 2A–H,L of the main text, and in Fig. S3A,B,D, is a mixture of two acrylate polymer components, each obtained from Sigma Aldrich. Bisphenol A glycerolate (1 glycerol/phenol) diacrylate (BPAGDA) was mixed at 75:25 wt% with poly(ethylene glycol) diacrylate (PEGDA) (average $M_n = 250$ g/mol). The viscosity of this polymer mixture was determined via cone-and-plate rheometry (TA Instruments AR 2000) to have a value of approximately 5200 cP at a steady strain rate of 1/s, falling to approximately 4700 cP in the shear strain rate range 10/s to 100/s. A type 2 photoinitiating system consisting of the photoinitiator camphorquinone (CQ) and co-initiator ethyl 4-dimethylaminobenzoate (EDAB) were added to the polymer formulation at 1:1 ratio by weight. The molar concentration of CQ in the resin formulation was 5.2 mM, selected to achieve an appropriate absorptivity of the resin (see Section S5). CQ and EDAB were also obtained from Sigma Aldrich.

Additionally, a 7:1 mixture of BPAGDA with 250 g/mol PEGDA was used to print the part shown in Fig. S3E. The photoinitiator content was the same as for the 3:1 mixture described above. This mixture was measured to have a considerably higher viscosity of $93,000 \pm 5,000$ cP. To provide an intuitive sense of how viscous these materials are, Movie S5 shows the flow under gravity of the 3:1 and 7:1 BPAGDA/PEGDA formulations.

S2. Hydrogel material

The hydrogel material used in Fig. 2I–K and in Fig. S3C is a gelatin methacrylate (GelMA) polymer obtained from Advanced Biomatrix (San Diego, CA) and dissolved 10% w/v in phosphate buffered saline. A different photoinitiator system was used for hydrogel printing because CQ has poor solubility in water. The photoinitiator used for hydrogel printing was a two-part visible light initiator consisting of tris(2,2-bipyridyl)dichlororuthenium(II) hexahydrate (Ru) and sodium persulfate (SPS) (32). Ru and SPS were mixed at concentrations of 2 mM and 20 mM respectively into the GelMA hydrogel. Hydrogel samples were cooled in a refrigerator to 2–5 °C to induce reversible thermal gelation and render the samples solid before photocrosslinking with CAL.

S3. Other materials

A broader range of materials including photoinitiators phenylbis(2,4,6-trimethylbenzoyl)phosphine oxide (Sigma Aldrich), bis(η 5-2,4-cyclopentadien-1-yl)-bis(2,6-difluoro-3-(1H-pyrrol-1-yl)-phenyl) titanium (Irgacure 784, BASF) and the polymer pentaerythritol tetraacrylate (PETA) have also been also utilized for fabrication with CAL. Those results are not included in the present work.

S4. Projection systems

Three projectors were used as illumination sources:

(1) An off-the-shelf commercial “digital light processor”-based (DLP) projector (Optoma ML570). This source has a pixel resolution of WXGA standard (1280×800 pixels). An $f = 75$ mm focal length lens was placed in front of this projector to focus the output image approximately at the center of the resin container with a depth of focus larger than the container. Structures of BPAGDA/PEGDA were printed using the blue channel (nominally 455 nm) of this source.

(2) A second DLP projection system with a similar lens was used for printing of additional BPAGDA/PEGDA and GelMA samples. This system utilized a DLP Lightcrafter 4500 projector from Digital Light Innovations (DLI), also with WXGA resolution. BPAGDA/PEGDA resins were patterned using the blue color channel. The green color channel was used for GelMA hydrogel samples.

(3) An additional Lightcrafter 4500 projector was used, customized by Wintech with a 405 nm source having a quoted optical output power of 5.5 W. This projector also had WXGA resolution. This 405 nm source was used to print structures in BPAGDA/PEGDA resins, including those shown in Fig. 1F–G, Fig. 2F,G, H, L and Fig. S3E–H.

All projection systems were controlled via custom MATLAB scripts and programmed to output patterned intensity images using the relevant color channel. Intensity spectra of the blue and green channels of projector (1) were obtained using a Thorlabs CCS200 spectrometer and are shown in Fig. S1. Additional geometries printed by these systems are shown in Fig. S3, and preliminary demonstrations are in (33) and (34).

Resin was contained in cylindrical glass vials with diameters in the range 1–5 cm. Each vial was rotated about its longitudinal axis using a Thorlabs PRM1Z8 motorized precision rotation mount or equivalent, with a 3–25 °/s rotation rate. The illuminated portion of the vial was immersed in a fluid with the same refractive index as the uncured resin—typically by using resin without photoinitiator. The index-matching fluid was contained in a transparent rectangular box, two of whose faces were perpendicular to the light propagation direction to minimize beam refraction. In all material formulations, the oxygen content was allowed to equilibrate prior to processing by storing the material in a container exposed to room air for several days.

S5. Absorption characterization

The concentration of the photoinitiator molecules in each polymer was selected to give reasonable absorbance at the illuminating wavelength. To set the photoinitiator concentration, absorbance values for the 3:1 BPAGDA/PEGDA and GelMA photoinitiator–resin mixtures were measured using UV-VIS spectrophotometry (Shimadzu UV-1280). Absorbance is defined in Eqn. S5, where $A(\lambda)$ is the absorbance at a particular wavelength of illumination, $T(\lambda)$ is the transmittance at that wavelength and $\Phi(\lambda)$ is the photon flux at the same wavelength. The subscripts i and t refer to, respectively, the flux incident on the material volume and the transmitted flux:

$$A(\lambda) = \log_{10} \left(\frac{\Phi_i(\lambda)}{\Phi_t(\lambda)} \right) = -\log_{10}(T(\lambda)). \quad (\text{S1})$$

Measurements were taken from a rectangular cuvette volume with path length, l , of 10 mm. From this measurement, the molar absorptivity $\epsilon(\lambda)$ of the photoinitiator was extracted, according to Eqn. (S2), where $[\text{PI}]$ is the molar concentration of the photoinitiator in solution:

$$A(\lambda) = \epsilon(\lambda) * [\text{PI}] * l. \quad (\text{S2})$$

The intensity $I(z, \lambda)$ of light inside the photosensitive material is modeled as decaying exponentially with propagation distance z , in accordance with the Beer–Lambert Law. Where the incident surface intensity is $I_0(\lambda)$, and adopting a change of base of logarithm, intensity can be expressed as:

$$I(z, \lambda) = I_0(\lambda) e^{-2.3\epsilon(\lambda)[\text{PI}]z} = I_0(\lambda) e^{-z/D_p}. \quad (\text{S3})$$

Here, $D_p = 1/\alpha$ is the *penetration depth*. Absorption spectra of the 3:1 BPAGDA/PEGDA and GelMA material formulations are shown in Fig. S1, along with the corresponding normalized intensity profiles for the relevant color channel in the projection hardware used. By illuminating off the absorption peaks, $[\text{PI}]$ can be high enough to provide enough photoinitiator to complete curing even while offering the low required absorption. The emission spectrum of the 405 nm source lies even further from the CQ absorption peak than the 455 nm source, which further benefits the process.

From the spectrophotometer measurements, the penetration depth of the 3:1 BPAGDA/PEGDA mixture was found to be $D_p = 2.2$ cm at the peak illumination wavelength of 455 nm, while that of the GelMA mixture was found to be $D_p = 0.4$ cm at the peak illumination wavelength of 520 nm. These penetration depths are on the same order as the container radii used, which, as we shall see in Section S18, makes the materials well suited to rapid printing while delivering the required 3D printing capability.

S6. Resin response calibration

To understand the response of 3:1 BPAGDA/PEGDA resin to incident illumination in the system, a series of calibration tests was performed. The CAL system hardware of Fig. S2A was used. A static image, shown in Fig. S2C, was projected toward the material volume as the volume rotated. The projected image consisted of a vertical array of circular patterns, each with a different programmed value of intensity. A video of the material volume curing was taken through a side window of the apparatus as shown in Fig. S2B. Each circular image generates a structure on the central axis of the build volume. By monitoring formation of these structures, the exposure time required for the onset of curing, or inhibition time t_{inhb} , was extracted through image processing on the video frames. Figure S2D shows the reciprocal of t_{inhb} , or average rate of inhibitor consumption during the inhibition phase, plotted versus incident intensity in each circular image.

The results follow a reasonably linear trend for the range of intensities used for curing, albeit with a small implied threshold intensity of ~ 0.2 mW/cm². We attribute this threshold to the diffusion of oxygen to the center of the vial from its less-exposed periphery, replenishing the inhibiting species effectively indefinitely at extremely low intensities. In any case, these findings approximately validate the assumption of linear recording of exposure dose in the projection computation. Linear regression was performed on data averaged from four trials (three trials for the highest intensity) to produce a best-fit line with $R^2 = 0.9874$, plotted in Fig. S2D.

From these data, a required dose of $D_{c0} = 4.9 \times 10^{22}$ photons/m³ for the onset of visible curing is extracted using the relationship:

$$D_{c0} = \frac{\alpha e^{-\alpha R_c}}{GE_p} \quad (\text{S4})$$

where $\alpha = 1/D_p = 46$ m⁻¹ from Section S5, $R_c = 7.5$ mm is the radius of the cuvette used for the exposure experiments, $G = 0.00153$ s⁻¹ m² W⁻¹ is the gradient of the $(1/t_{\text{inhb}})$ –intensity relationship fit in Fig. S2D, and E_p is the energy of a 455 nm photon.

S7. Post-processing

For some prints, a heating step was used to reduce the viscosity of uncured material and aid in its removal. Vials containing the printed part and uncured material were placed in a temperature-controlled water bath. Hydrogel samples were placed in a 37 °C water bath until the unconverted material was pourable (after about one minute). BPAGDA/PEGDA samples were heated in a water bath at 80 °C for 5–10 seconds.

S8. Regeneration of resin

The following protocol was used to replenish dissolved oxygen in unconverted material from a previous build (print-run), to enable re-use of the resin for a successful second build of the same part under identical exposure conditions.

1. Fresh 3:1 BPAGDA/PEGDA with 5.2 mM CQ/EDAB was mixed as described above. A first part was printed (in our demonstration, the *Thinker* geometry, with a print time of 5 minutes).
2. The vial containing the printed part and surrounding unconverted material was submerged in a water bath at 60 °C for 5–20 s to reduce the viscosity of the unconverted material.
3. Unconverted material was poured into a Petri dish on a heated plate (heated to 60 °C). The resin spread out on the Petri dish, providing a large surface area for an increased rate of oxygen diffusion into the material from the ambient air.
4. The heated material was left exposed to air in the Petri dish for 30 minutes.
5. Material was poured into a fresh glass vial for printing.
6. Material was allowed to cool to room temperature.
7. A second build of the same geometry was executed using exactly the same exposure time of 5 minutes.

Results (Fig. S4) show that the two print runs yield indistinguishable geometries after equal exposure times. Because the only regeneration step taken was to replenish

oxygen, we conclude that there is no evidence that sub-threshold exposure or the subsequent regeneration process changes the polymer properties significantly or that photoinitiator concentration is sufficiently depleted to affect the resin's reusability for at least one re-use.

S9. Printing of opaque material

To print an opaque component, a dye, crystal violet (Sigma Aldrich), is mixed into 3:1 BPAGDA/PEGDA resin with the same formulation as in Section S1. Crystal violet has very low absorptivity at the photocuring wavelength used, 405 nm, allowing the printing illumination to penetrate, but absorbs strongly through much of the visible spectrum (Fig. S1C), giving the printed component a deep blue/violet color. A dye concentration of 0.003% w/v was used. Fig. 1F–G of the main text and Fig. S5 show an example of a *Thinker* printed with dyed resin next to the same geometry printed with undyed resin. We anticipate other coloring schemes being possible with other dyes.

S10. Characterization of surface smoothness and dimensional fidelity of printed components

Very smooth surfaces are observed in the samples shown in Fig 2I–K (GelMA) and Fig 2L (3:1 BPAGDA/PEGDA). In Fig 2I–K, the way in which the samples reflect light in the photos shows that they are very glossy: for example, they show clearly reflected images of the lamp and bulb that were used to illuminate them. These reflections are indicative of an optically smooth surface.

In Fig 2L, which shows a component with flat and convex curved surface regions, one can clearly visualize a page of text through the component. A gentle lensing effect is seen in the curved portion of the component. This component was then sputtered with ~100 nm gold and measured with a Keyence VK-X250 laser microscope (408 nm laser, 10x objective NA = 0.3). Two separate 300 μm \times 500 μm zones of the convex region were characterized, and were found to have arithmetic mean roughnesses, R_a , of 4.4 μm and 7.2 μm , and average peak–valley roughnesses, R_z , of 19.6 μm and 36.7 μm respectively. The nominally planar region of the component was also characterized, and the one dust-free zone measured yielded R_a = 1.5 μm and R_z = 17.4 μm . The component shown in Fig 2G was also measured on its top surface mid-way between the wings, resulting in R_a = 1.0 μm and R_z = 15.0 μm . A third component, a lens printed using CAL in 3:1 BPAGDA/PEGDA without post-curing (not shown in the figures) was found to have R_a = 0.8 μm and R_z = 4.6 μm . Therefore, surface roughnesses produced by CAL exhibit a range, but can be sub-micron.

We created an additional test structure to facilitate comparison of dimensional measurements of a printed component with the associated computer-aided design (CAD) model (Fig. S20A–C). Using a calibrated bright-field white-light microscope, we determined that printed dimensions of this 3:1 BPAGDA/PEGDA component deviated by 0.5–8.8% in magnitude from the designed values. We also measured the radius of the tip of the tail-fin of the airplane of Fig 2G to be 200 μm (Fig. S20D–E). This radius is in fact smaller than the radius drawn in the CAD file (400 μm). The increased sharpness may result from the non-linear dose response of the photopolymer and oxygen diffusion towards this isolated feature during printing.

S11. Mechanical characterization of printed components

To confirm that the use of CAL does not result in significantly different mechanical properties from a more conventional processing route, we conducted nanoindentation measurements (Hysitron TI-950 Triboindenter, Hysitron, Eden Prairie, MN, USA) to characterize Young's modulus of cylindrical 3:1 BPAGDA:PEGDA samples processed in four different ways:

1. Formed by CAL alone using the Wintech LC4500 projector at 405 nm for 3 minutes, with no post-printing exposure;
2. Formed by the same CAL process as in case (1), but followed by a 20-minute static flood exposure using the Wintech LC4500 projector at 405 nm and 100% intensity to increase the degree of crosslinking;
3. As (2), but with a 90-minute static flood exposure instead of 20 minutes.
4. A static flood exposure of 90 minutes using the Wintech LC4500 projector at 405 nm and 100% intensity, without any prior exposure via CAL.

Cases 1–3 represent different stages of an anticipated CAL processing flow: (1) immediately after removal from the printing apparatus, and (2 or 3) after a flood exposure of varying length to increase or complete crosslinking. (A post-printing flood exposure is typical in layer-based stereolithography processes.) Case 4 represents a benchmark case where crosslinking can be assumed to be very close to complete because of the long exposure time, yielding a component with the highest stiffness achievable for the material via any processing route.

Young's modulus was extracted from load–displacement results using the Johnson–Kendall–Roberts method (35). The results (Fig. S6A–B) show a Young's modulus of 15.3 ± 1.1 MPa ($N=6$) after CAL printing plus a 90-minute flood exposure, and 13.8 ± 3.5 MPa ($N=6$) after the benchmark 90-minute flood exposure without prior CAL exposure. Young's modulus after CAL exposure and before post-curing was 0.28 ± 0.06 MPa ($N=15$), indicating that crosslinking has just begun when the geometry forms, and 8.84 ± 1.86 MPa ($N=15$) after 20 minutes of post-curing. All uncertainties reported here are standard deviations.

We also conducted tensile testing of three CAL-printed dogbone samples following the ASTM D638 Type V standard. In this case, samples received 45 minutes' postcuring using the Wintech LC4500 projector at 405 nm. These tests (Fig. S6C–D) showed an engineering tensile stress at failure of 18.0 ± 6.3 MPa SD ($N=3$), with the best-performing sample exhibiting a failure stress of 24.9 MPa at an elongation of 55%. These results compare well with a commercially available AM flexible polyurethane resin, which is reported to have an ultimate tensile strength of 29 ± 1 MPa (36). Young's modulus of our dogbone samples was determined to be 78.5 ± 28.8 MPa SD ($N=3$), suggesting that bulk material properties may differ from those at the surface as measured by nanoindentation.

These findings indicate that CAL followed by a flood exposure can produce parts with mechanical properties comparable to other acrylated AM resins processed in other ways. It should be noted that these results are for a BPAGDA:PEGDA mixture, and neither this material nor its processing conditions have been at all optimized for mechanical performance. The duration of the flood exposure needed could be shortened

by increasing the intensity of illumination via a dedicated light-curing oven, as used in conjunction with industrial stereolithography tools.

Supplementary Text

S12. Optimization algorithm

The exact solution calculated by inverting the exponential Radon transform $T^*_{-\alpha}[g * W](\mathbf{r}, z)$ is not physically realizable due to negatives in the filtered projections $g * W$. However, the exact solution presents a useful initialization for the iterative optimization procedure. In fact, the threshold allows for a trivial solution in every case: subtract $\min(g * W)$ from the exact back-projections, ensuring that the dose profile is entirely positive. However, this makes the contrast between cured and uncured target regions impractically low for most resin chemistries and the geometry becomes very sensitive to small variations in dose.

If we remove the thresholding nonlinearity in the forward model, the positivity-constrained optimization becomes convex with linear constraints, and the solution can be directly written using the Kuhn-Tucker conditions as: $\Pi_S(g * W)$, the projection of the exact solution (with negative excursions) into the constraint set S . Essentially, the solution to the convex problem is arrived at by simply setting the negatives in the projection image to zero. However, this yields an energy dose distribution that produces printed objects that fail to satisfactorily match the desired geometry.

Instead, we adopt a more robust approach based on iterative optimization that results in a dose distribution with greater contrast. The iterative algorithm is initialized with: $\Pi_S(g * W)$, the solution to the convex problem without the thresholding non-linearity. Projected gradient descent updates incorporating the threshold chemistry are then used to iteratively improve projection estimates. The threshold dose is continually updated in each iteration based on Otsu's method (37) to minimize the variance of voxels in each class (solidified and non-solid). This is a simple segmentation technique borrowed from computer graphics. We use the following first-order iterative scheme based on a finite difference approximation to the gradient to update the projections:

Algorithm 1:

1. Procedure: CALopt
2. $p \leftarrow T_\alpha[T]$: projection of the target geometry
3. $p_0 \leftarrow \Pi_{S_+}(p * W(r))$: initialize by projecting exact solution into constraint set
4. $n \leftarrow 0$
5. while $n < maxIter$ do
 1. $n \leftarrow n + 1$
 2. $F_n \leftarrow T^*_{-\alpha}[p_{n-1}]$: unfiltered backprojection to obtain dose
 3. $d_n \leftarrow \text{Otsu}(F_n)$: threshold calculation
 4. $T_n \leftarrow 1/3 * (\Theta(F_n, d_n) + \Theta(F_n, d_n * (1 - \delta)) + \Theta(F_n, d_n * (1 + \delta)))$: (robust thresholding of dilated, eroded and nominal dose distributions)
 5. $\delta_n \leftarrow T_\alpha[T_n - T]$: gradient formed from projection of the difference

6. $p_n \leftarrow \Pi_{S_+} (p_{n-1} - \gamma \delta_n)$: projected gradient descent update

The tunable parameters γ and δ are chosen heuristically in order to improve convergence characteristics. Several improvements to the current algorithm are possible in future work, including the implementation of a more suitable merit function than just least-square error. A more suitable merit function has been proposed by Zhang *et al.* (22), and differentiates between dark and bright voxels, penalizing the undesired polarity with a truncated square function.

S13. Transformation to external projections

The computation of projections has been described for the projection space defined on radial cuts passing through the center of rotation of the vial. Here we describe the simple algebraic transformation required to obtain external projections from the optimized projections calculated through these radial cuts.

The standard definition for the exponential Radon transform, as described in the text in Eqn. (1) is based on the internal projections defined on the dashed line as shown in Fig. S8:

$$f(\mathbf{r}, z) = \int_{\theta=0}^{2\pi} g(\mathbf{r}, \hat{\theta}, \theta) e^{-\alpha r \cdot \hat{\theta}_\perp} d\theta \quad (\text{S5})$$

However, the projections are produced by a projector exterior to the domain. The transformation to the exterior is dependent on the depth traveled through the resin at each radial position, with a radially dependent amplifying factor as follows:

$$g_{ext}(\mathbf{r}, \hat{\theta}, \theta) = g_{int}(\mathbf{r}, \hat{\theta}, \theta) e^{\alpha(R^2 - (\mathbf{r} \cdot \hat{\theta})^2)^{0.5}} \quad (\text{S6})$$

where R is the radius of the container. Qualitatively, the external projections need to be amplified more at the center of the container, where the rays of light travel a greater distance. This factor can be ignored if the radius is very large compared to the print object size, or if the attenuation is small.

S14. Inversion of the exponential Radon transform

This section further explains the frequency domain back-projection filter, including why frequencies below α are zeroed. What follows is a summary of the derivation used by Tretiak and Metz (24). The unfiltered backprojection can be expressed as follows in the notation of the main manuscript, where \hat{T}_α^* is the 2D inverse Fourier transform followed by amplified backprojection, $\hat{T}_{-\alpha}$ is the attenuated projection followed by 2D Fourier transform, and $f_T(\mathbf{r})$ is the target geometry at a particular z-slice:

$$\hat{T}_\alpha^* \{ \hat{T}_{-\alpha} [f_T(\mathbf{r})] \} = PSF(\mathbf{r}) * f_T(\mathbf{r}) \quad (\text{S7})$$

where $PSF(\mathbf{r})$ is the point spread function of the unfiltered backprojection. In other words, the unfiltered amplified backprojection of the exponential Radon is a linear shift

invariant operation on the target geometry, which has the effect of convolving it with a particular kernel $PSF(\mathbf{r})$. This kernel depends on the absorption coefficient α , and its functional form can be expressed as:

$$PSF(\mathbf{r}) = 2 \frac{\cosh(\alpha|\mathbf{r}|)}{|\mathbf{r}|} \quad (S8)$$

Then, the inversion operation requires a deconvolution, which can be expressed in the backprojection Fourier space (conjugate to radius) as the ramp filter $\widehat{W}_\alpha(k)$:

$$\widehat{W}_\alpha(k) = |k| \text{ if } |k| > \alpha, \text{ else } 0 \quad (S9)$$

The entire inversion process can then be expressed as a modification of the unfiltered backprojection as:

$$f_T(\mathbf{r}) = \widehat{T}_\alpha^* \{ \widehat{W}_\alpha \cdot \widehat{T}_{-\alpha} [f_T(\mathbf{r})] \} \quad (S10)$$

We note that the filter reduces to the standard ramp filter for $\alpha = 0$. The key point here is that the point spread function depends on the absorption coefficient, and its effect can be undone by using a particular ramp filter that is different from the standard radon transform and also has some dependence on the absorption coefficient. Further mathematical details to arrive at the particular functional form of the ramp filter can be found in Tretiak's and Metz's original paper (24). Kuchment (38) has a more detailed description of the inversion procedure.

S15. Influence of the number of projection angles

Based on the tomographic framework the angular sampling requirement is set by: $\delta\theta \leq x/R$, where x is the radial sampling period and R is the radius of the geometry. This can be derived by setting a requirement on the maximum frequency space separation between angular Fourier slices (see ref. (20) in the main text, Chapter 5 ‘Aliasing Artifacts and Noise in CT Images’). If this Fourier slice separation is exceeded, we begin to observe strong spatial artifacts (spatial aliasing) that corrupt the reconstruction. The same formula can also be used to relate the number of angular samples N_θ to the number of spatial samples across the field of view, N_r : $N_\theta \geq \frac{\pi}{2} N_r$. Therefore, it turns out that three beams is severely insufficient when a large number of radial samples (~ 500 – 1000 in the current work) are used. In fact, a much better number of angular samples would be 800 – 1600 . By using three beams, only three slices of the 3D Fourier space are sampled. This discards significant frequency space information and leads to poor reconstruction quality (Fig. S17).

We study the dependence of reconstruction quality on the number of beams using a scalar spatial similarity metric, the Jaccard index. The Jaccard index J produces a metric $[0, 1]$ to compare the reconstructed volume G_R with the target volume G_T . The Jaccard index is defined as the ratio of the volume of the intersection between the target and reconstructed geometry to the volume of the union of the target and reconstructed

geometries: $J = \frac{|G_R \cap G_T|}{|G_R \cup G_T|}$. The Jaccard index is unity when the two geometries overlap perfectly—which is the desired case. Typically, a Jaccard index above 0.75 may be considered good overlap, with 0.9 being desirable. In our analysis, the target geometry is obtained from the STL file, and can be reconstructed with very high accuracy ($J \sim 1$) when the number of angular samples is high, and the filtered backprojection (FBP) algorithm is used. The only source of error in this case is due to sampling, which needs to be chosen finely enough to represent the geometry. However, FBP leads to projections with negative values (as explained in the main text), which are not physically realizable in a light intensity-based implementation. On the other hand, we lose fidelity when we do not perform the filtering operation. This obstacle has been overcome by using a positivity-constrained gradient descent method to solve for the projections as described in eqn. 4 of the main text, and leads to a good Jaccard similarity index when the number of angular samples (*i.e.* number of beams) is high.

The Jaccard similarity index has been plotted against the number of beams for three cases: unfiltered backprojection (blue curve), optimized backprojection with positivity constraint (orange), and filtered backprojection without constrained values (yellow) (Fig. S17C,D). As expected, since the filtered backprojection operation perfectly inverts the Radon transform (other than small sampling error), the Jaccard similarity is near unity at fine angular sampling for all the geometries. The unfiltered backprojection performs quite poorly (blue), but with appropriate optimization, we again recover good fidelity, as seen in the bold orange curve. Note that a binary thresholding method has been used to obtain the binary geometry from the continuously distributed three-dimensional dose. The threshold was chosen to maximize the Jaccard similarity with the target geometry, for every angular sampling number.

We emphasize that when insufficient angular samples are used, the Jaccard similarity index using any of the methods is quite low. Typically, with three beams, the geometry is nearly unrecognizable. With ten beams, the object becomes recognizable in some cases, but lacks finer features. Finally, when the number of angular samples is on the order of 1000 or higher, we start to obtain good reconstruction fidelity.

We also attempted to construct the ‘Thinker’, dental aligner and gyroid geometries by using beams propagating in three orthogonal directions, to simulate the method of (9) and rule out the possibility that that method could reconstruct these complex geometries. This approach leads to very poor, virtually unrecognizable reconstructions with Jaccard indices ranging from 0.35 to 0.67 (Fig. S18). Therefore, whether three beams are directed orthogonally (as in (9)) or in 120°-offset directions about the axis of a print volume (as in a grossly under-sampled implementation of CAL), successful reconstruction of arbitrary geometries appears impossible.

S16. Print resolution (point spread function) analysis

The point spread function (PSF) of the rotating optical system determines the smallest printable object. We calculate the PSF of dose distribution by accounting for the pixel size of the projector (δP), the rotation rate of the vial (Ω), the frame rate of the projector (f_p) and the optical parameters of the low-NA single lens imaging system. The nonlinear dose-response of material conversion during the curing process is not

accounted for in this analysis, making this a conservative estimate of the achievable resolution.

In order to calculate the PSF, the blurred sinogram $\hat{g}(r, \theta)$ corresponding to a target point object: $f_T(\mathbf{r}) = \delta(\mathbf{r} - \mathbf{r}_0)$ is back-projected into the volume:

$$F(\mathbf{r}) = \int_{\theta=0}^{2\pi} \hat{g}(r, \theta) d\theta \quad (\text{S11})$$

This is an appropriate model for the weakly attenuating resin formulation used to generate the geometries described in this work. The blurred sinogram is obtained by imposing the resolution limitations with box convolutions on the Radon transform $g(r, \theta)$ of the point object. Note that we use the unfiltered Radon transform rather than the backprojection-filtered version ($g * h(r)$) in order to maintain positivity of the projected signal. The two convolution operations corresponding to a finite spatial pixel size and finite angular resolution are imposed as:

- finite pixel size: $\hat{g}(r, \theta) = g(r, \theta) * B(r/\delta P)$
- finite angular resolution: $\hat{g}(r, \theta) = \hat{g}(r, \theta) * B(\theta/\delta\theta)$

where the box convolution filter $B(r/r_0) = I_{|r| < r_0/2}$ is unity over a spatial range (or angular range respectively) of r_0 . The spatial pixel size at the image plane δP determines the support of the box filter. The angular resolution $\delta\theta = \Omega/f_p$ is essentially the angular range over which one frame is projected, and is limited by the frame rate of the projector. In the particular implementation described in this work, $\delta P = 32 \mu\text{m}$, $3^\circ/\text{s} \leq \Omega \leq 25^\circ/\text{s}$, and $f_p = 25 \text{ Hz}$, leading to an angular resolution $0.12^\circ \leq \delta\theta \leq 1.0^\circ$.

The backprojected dose distribution $F(\mathbf{r})$ (un-thresholded) corresponding to three points in the target geometry at different radii from the center of rotation $(0, 0)$ are shown below in Fig. S9. The rows correspond to a fixed angular resolution, and columns correspond to a fixed spatial pixel size. We note that the effect of the finite spatial pixel is to create a circularly symmetric point spread function, as can be noted from the PSF at the origin in each of the images. The angular resolution has the effect of introducing a tangential blur, as can be seen from the top right and bottom left PSF in each of the frames, with an artificially large angular resolution being used to exaggerate the effect. The tangential blur increases with the radius of the PSF center from the center of rotation, implying that the PSF is spatially varying within the print volume. The effect of the angular resolution can be minimized by using a high frame rate and slow rotation rate.

S17. Modulation transfer function (MTF) model

The PSF analysis of Section S16 provides valuable information about CAL's capabilities in a form that is commonly used to characterize optical systems. Another important characteristic of lithographic systems is the *modulation transfer function* (MTF), which describes the system's ability to impart to the target material a pattern with adequate intensity variation and a given spatial period. Where the distribution of optical dose along some spatial coordinate x' is $D(x')$, the MTF is defined as:

$$\frac{\max D(x') - \min D(x')}{\max D(x') + \min D(x')}.$$
(S12)

We describe here a computational analysis of how the MTF for a one-dimensional periodic pattern depends on the following attributes:

- The ratio d/p of the width, d , of one projected pixel to the spatial period, p , of the desired pattern (as in the projection computation algorithm, divergence of the beam is assumed negligible);
- The dimensionless tangential velocity $\Omega c/f_p p$ of the photosensitive material at the patterning location (Ω is the container's rotational velocity, c is the radial position, and f_p is the frame-rate of the projector);
- The dimensionless radial position, c/R , of the pattern within the photosensitive volume where R is the radius of the container;
- The angle β between the longitudinal axes of individual features of the pattern and the radial direction of the print volume ($\beta = 0$ corresponds to 'spokes of a wheel' while $\beta = 90^\circ$ corresponds to concentric circles). Locally, features are assumed parallel and without curvature.
- The fraction of the container's rotation time during which the target material is actually being exposed (we show that for each combination of the above parameters, there is a trade-off between MTF and total average dose received per revolution, because some values of θ give higher MTF than others).

Spatial variables are illustrated in Fig. S10B. We assume that the material's absorption coefficient has the optimum of $\alpha = R$ that is derived in Section S18 below. The analysis has two phases:

- (1) For a range of relevant combinations of d/p , $\Omega c/f_p p$, and β , evaluate MTF for each of a finely spaced set of azimuthal positions θ , varying from 0 to 2π .
- (2) Combine the MTFs from phase (1) with knowledge of resin absorbance at each $(c/R, \theta)$ combination to show how the overall effective MTF depends on c/R and the fraction of the resin container's rotation during which the features are being exposed to light.

Phase 1. The desired (target) one-dimensional periodic dose pattern $D_t(x')$ is a square-wave with pitch p and duty-cycle 50%. Where $u(\cdot)$ is the Heaviside step function:

$$D_t(x') = \sum_{i=-\infty}^{\infty} u(x' - ip) - u\left(x' - ip - \frac{p}{2}\right).$$
(S13)

For a given situation, both the finite-frequency refreshing of the projector image and the finite pixel size may limit MTF and these factors must be considered together.

The refresh-rate of the projector and the rate at which the projected image sweeps past periods of the target pattern rarely have an integer ratio, so these frequencies will often therefore 'beat' in complex ways with much lower frequencies. To provide an approximation to the cumulative dose received while still using a reasonably-sized

simulation domain, we therefore consider a number, η , of short bursts of projector-refresh events, each of which simulates the photosensitive material moving relative to the projector by at least one pattern period p , and further if twice the projected pixel size exceeds the target pattern pitch. Each burst consists of ζ refresh events where:

$$\zeta = N_s \max \left[1, \text{Ceil} \left(\frac{2d}{p|\cos(\theta + \beta)|} \right) \right], \quad (\text{S14})$$

$$N_s = \left| \text{Round} \left(\frac{f_p p}{\Omega c \cos \beta} \right) \right| \quad (\text{S15})$$

and the spatial offset between samples in the x' direction is

$$b = \frac{p}{N_s}. \quad (\text{S16})$$

The operator $\text{Round}(\cdot)$ returns the closest integer to its argument and $\text{Ceil}(\cdot)$ returns the smallest integer greater than its argument. Each of the η bursts is also assigned an additional small spatial offset $x'_{0,j}$ between the pixels and the target pattern:

$$x'_{0,j} = \frac{pj}{\eta N_s} \quad (\text{S17})$$

where $\eta = \text{Round}(256/N_s)$. In this way, the effects of ‘beating’ between the projector refresh cycles and the target pattern are accounted for and effectively averaged out.

At each projector-refresh event, it is assumed that the pixels of the projector are set to project an intensity proportional to whatever value the target dose distribution $D_t(x')$ happens to have at the center of the pixel. Since $D_t(x')$ is binary as defined, so is the projected intensity. This binary intensity value is then held constant until the next such ‘sampling’ event. This sampling function takes account of the angular displacement between the projection direction and the pattern orientation, and is:

$$S(x'') = \sum_{i=-\infty}^{\infty} \delta \left(x'' - \frac{id}{|\cos(\theta + \beta)|} \right). \quad (\text{S18})$$

The intensity from a single pixel projected on to the x' axis is assumed to have uniform intensity and sharp edges:

$$P(x') = |\cos(\theta + \beta)| \left[u \left(x' + \frac{d}{2|\cos(\theta + \beta)|} \right) - u \left(x' - \frac{d}{2|\cos(\theta + \beta)|} \right) \right]. \quad (\text{S19})$$

The blurring effect of the material’s motion relative to the projector is captured with a ‘hold’ function as follows:

$$H(x') = \frac{f_p}{\Omega c \cos \beta} \left[u(x') - u \left(x' - \frac{\Omega c}{f_p} \cos \beta \right) \right]. \quad (\text{S20})$$

The dose reaching the material is therefore approximated as:

$$D(x') = \frac{1}{\zeta\eta} \sum_{j=1}^{\eta} \sum_{i=1}^{\zeta} [D_t(x') S(x' - ib - x'_{0,j})] * H(x') * P(x') \quad (\text{S21})$$

where $*$ denotes convolution in x' . The convolutions are computed approximately in discrete space by multiplying fast Fourier transforms of the variables. A 4096-point domain is used, corresponding to a distance of $16p$ in the x' direction. MTF can be computed from the output of (S21) using the relation in (S12).

Phase 2. To obtain a finite dose, a particular patterned location needs to be exposed over a finite range of θ as it rotates in the printing volume. As shown above, however, MTF varies with θ . Therefore, there is a trade-off between average dose delivered per revolution and MTF. MTF is highest when $\cos(\theta + \beta) = \pm 1$, meaning that the longitudinal axes of the desired features are parallel to the light propagation direction. Conversely, MTF is lowest when $\cos(\theta + \beta) = 0$, and, in general, MTF values fall as $|\cos(\theta + \beta)|$ reduces.

The cumulative dose delivered over a specific set of θ values is found by superimposing the dose profiles obtained in (S21) for those values of θ :

$$D_{cum}(x', N_\theta) = \sum_{\xi=1}^{N_\theta} e^{-\alpha w(c, \theta_\xi)} D(x', \xi) \quad (\text{S22})$$

subject to the sorting constraint that

$$|\cos(\theta_\xi + \beta)| > |\cos(\theta_{\xi+1} + \beta)| \quad (\text{S23})$$

and where $w(c, \theta_\xi)$ is the propagation distance through the resin, given in (S38). As N_θ increases, the components added to $D_{cum}(x', N_\theta)$ have progressively smaller MTF values.

Results. Fig. S10A shows how MTF depends on the resolution-limiting effect of the pixel size relative to the feature pitch, d/p , and also on the blurring effect of the tangential velocity relative to the projector refresh rate and the feature pitch: $\Omega c/f_p p$. These results are shown for a single representative azimuthal position: $\theta = 0$. Where the projector's spatial sampling of the desired pattern satisfies the Nyquist sampling criterion (*i.e.* $d/p < 0.5$) and $\Omega c/f_p p$ is very small so that motion blurring is not an issue, a perfect MTF of 1 is obtained. As blurring becomes more significant or the pixel size grows relative to the desired pitch, the MTF does of course degrade, to value of zero at $d = p$. For values of $d/p > 1$, however, there is a periodic recovery of MTF, up to peak values of:

$$\frac{1}{2 \operatorname{Ceil}\left(\frac{d}{p}\right) - 1} \quad \text{when } \frac{d}{p} = k + 0.5 : k \in \mathbb{Z}. \quad (\text{S24})$$

These peaks correspond to pixel edges aligning perfectly with feature edges, with a pixel spanning an odd number of half pattern pitches. Although an MTF of at most $1/3$ can be obtained in this way (at $d = 1.5p$), this observation may provide a route to surprisingly

high-resolution patterning via careful control of the projector and use of a material with a sufficiently nonlinear dose response.

For context, the *critical* MTF (CMTF), which is the smallest acceptable MTF for successful pattern transfer, is a reducing function of the *contrast*, γ , of a photosensitive material:

$$\text{CMTF} = \frac{10^{1/\gamma} - 1}{10^{1/\gamma} + 1} \quad (\text{S25})$$

where γ represents how strongly nonlinear the material's dose response is:

$$\gamma = \frac{1}{\log_{10} \frac{D_{100}}{D_0}}. \quad (\text{S26})$$

Here, D_0 is the illumination dose at the beginning of conversion and D_{100} is the dose for close to full conversion. Typical photoresists optimized for high-performance microlithography have γ between 2 and 3, corresponding to a CMTF between 0.37 and 0.52.

Fig. S11, meanwhile, shows the trade-offs between MTF and normalized cumulative spatially-averaged dose. The normalized average dose for a particular value of N_θ is calculated as the average of $D_{cum}(x', N_\theta)$ over x' , divided by the spatial average of $D_{cum}(x', N_\theta)$ for the largest available value of N_θ , *i.e.* including all values of θ . These results show that circumferentially oriented features ($\beta = \pi/2$) offer the highest MTF under any circumstances, and are insensitive to rotational velocity in the range considered. Radially oriented features ($\beta = 0$) are the most challenging to print and lead to the lowest MTFs, while the intermediate value of $\beta = \pi/4$ shows intermediate performance.

For $\beta = 0$, the smallest relative radial positions yield highest MTF at a given $\Omega c/f_p p$, whereas for $\beta = \pi/2$ the highest MTF is obtained when $c = R$. This difference occurs because when $\beta = \pi/2$, some of the lowest MTF values occur for θ around π , and these unfavorable components are usefully suppressed when c/R approaches 1 and absorption of the light illuminating them is maximized with a propagation distance of $2R$. For $\beta = 0$, on the other hand, the most *favorable* MTF components occur when θ is 0 or π , so long peak propagation distances are undesirable and instead low c/R is preferable. It should be stressed that this discussion is based on constant $\Omega c/f_p p$ and d/p that are within the reasonable bounds shown in Fig. S11.

These trade-offs show that it may be desirable to illuminate a particular section of a pattern at a subset of θ values that offer higher overall MTF, at the possible expense of printing speed. The MTF values presented here are expected to be conservative because there may be superior grayscale sampling schemes that do not simply set each projector pixel to either the maximum or zero intensity based on sampling of the target pattern, as is assumed here. Indeed, our core projection generation algorithm creates grayscale patterns. On the other hand, the projection of *binary* intensity patterns from micromirror device-based projectors can be refreshed far faster (\sim kHz) than the projection of

grayscale patterns, which rely on pulse-width modulation and can currently only achieve typical video rates of a few tens of Hz.

In the present work, $f_p = 25$ Hz, $\Omega \leq 25^\circ/s$, $c \lesssim 0.015$ m, and the signals from the projector's 1280 pixels are directed into a width of approximately $2c = 30$ mm such that $d \approx 23\text{ }\mu\text{m}$. Under the most challenging conditions used, therefore, the dimensionless tangential velocity $\Omega c/f_p p$ rises to 0.5 at feature pitch $p = 0.52$ mm, in which case $d \ll p$. The top right-hand panel of Fig. S11 shows that for $\Omega c/f_p p = 0.5$ and $d \ll p$, MTF is still at least 0.8, even in the worst case of $\beta = 0$. By considering this simple case we see that the smallest feature widths printed experimentally in this work, of 0.3 mm, are expected to be well within the capabilities of the system at the operating point used.

In the z -direction, meanwhile, the resolution of the implementation presented is determined by the z distance over which the projector's pixels are distributed. Given axisymmetric projection optics, the z resolution is estimated as being equal to d , 23 μm . In future systems we envisage it being possible to achieve finer z resolution and/or larger print volumes by using micromirror devices with more pixels, multiplexing such devices, or dividing up the print volume into vertical ‘bands’ of, *e.g.*, several cm that would be sequentially exposed, without resorting to the sub-mm layering approach of presently available methods.

S18. Illumination times required for CAL vs. layer-by-layer techniques

As a first step towards comparing the achievable printing speeds of CAL to those of incumbent, layer-based processes, we consider the time needed to expose the photosensitive material to the dose required for solidification, D_c (photons absorbed per unit volume). We compare exposure times for CAL with those for two layer-based techniques. The first such process is projection stereolithography (PSL), in which a 3D part is built up in a sequence of discrete layers by projecting a 2D light pattern through a transparent window into resin (Fig. S12A). In PSL, the material is stationary during exposure and is translated in the z direction (normal to the window) between exposure steps (*e.g.* (28, 39, 40), Fig. S12C). The second comparison is with ‘continuous liquid interface production’ (CLIP), introduced by Tumbleston *et al.* (11), who proposed that motion in the z direction be continuous while the projected image is periodically updated to achieve a finite ‘slicing’ thickness (Fig. S13). In Section S19 we additionally consider the constraints on speed imposed on PSL and CLIP by hydrodynamic flow considerations in the resin, and then in Section S20 integrate the illumination and hydrodynamic analysis to compare overall print speeds for equivalent print volumes.

(a) *Exposure speed in PSL*

We first consider light penetration into the photosensitive material in PSL (Fig. S12). From the Beer–Lambert law (11, 12), the photon flux Φ_{PSL} is

$$\Phi_{PSL} = \Phi_{0,PSL} e^{-\alpha_{PSL} z}. \quad (\text{S27})$$

where α_{PSL} is the material’s absorption coefficient (inverse of penetration depth, D_p), $\Phi_{0,PSL}$ is the photon flux at the entry point to the absorptive material, and z is the

distance propagated by light through absorbing material. The photon absorption rate per unit volume is:

$$B_{PSL} = -\frac{d\Phi_{PSL}}{dz} = \alpha_{PSL} \Phi_{0,PSL} e^{-\alpha_{PSL} z}. \quad (S28)$$

In PSL, the exposure time $t_{c,PSL}$ required to cure a layer of thickness L is governed by the photon absorption rate at the location in the layer that lies furthest from the illumination source and where photon flux is therefore lowest. This propagation distance is $L + h_d$, where h_d is the thickness of the oxygen-inhibited dead-zone. The value of h_d may be zero in processes not relying on a permeable window, or may typically range up to values comparable to L . To meet or exceed a dose of D_c throughout the layer bring printed:

$$\begin{aligned} D_c &= \alpha_{PSL} \Phi_{0,PSL} t_{c,PSL} e^{-\alpha_{PSL}(L+h_d)} \\ \Rightarrow t_c &= \frac{D_c e^{\alpha_{PSL}(L+h_d)}}{\alpha_{PSL} \Phi_{0,PSL}}. \end{aligned} \quad (S29)$$

The value of α_{PSL} for which printing time is minimized, α_{PSL}^* , can be found by setting

$$\frac{dt_{c,PSL}}{d\alpha_{PSL}} = 0 = \left(\frac{D_c}{\Phi_{0,PSL}} \right) \left[\frac{\alpha_{PSL}(L + h_d) - 1}{\alpha_{PSL}^2} \right] e^{\alpha_{PSL}(L + h_d)} \quad (S30)$$

of which the only finite solution is $\alpha_{PSL}^* = 1/(L + h_d)$ and the optimized layer exposure time is

$$t_{c,PSL,\min} = \left(\frac{D_c}{\Phi_{0,PSL}} \right) e(L + h_d). \quad (S31)$$

Therefore if the printing speed is dominated by the exposure of resin, the speed is:

$$V_{ill,PSL} = \frac{L}{t_{c,PSL,\min}} = \left(\frac{\Phi_{0,PSL}}{D_c} \right) \frac{L}{L + h_d} e^{-1}. \quad (S32)$$

This speed relationship is illustrated in Fig. S12B. The above analysis is valid as long as the absorption of the resin comes entirely from dissolved photoinitiator (*i.e.* $\alpha_{PSL} = \alpha_{PI,PSL}$). If α_{PSL}^* implies a value higher than the maximum achievable $\alpha_{PI,PSL}$ (because of a solubility limit for example), there is no *speed* advantage to increasing α_{PSL} with dye in order to reach α_{PSL}^* , although this is commonly done to prevent ‘print-through’, *i.e.* the loss of layer resolution.

(b) Exposure speed in CLIP

In CLIP as described by Tumbleston (11), on the other hand, the part being printed moves continuously in the z direction (Fig. S13A) while the illumination pattern changes periodically. By adapting (S28) the rate of dosing is

$$\frac{dD}{dt} = -\frac{d\Phi_{CLIP}}{dz} = \alpha_{CLIP} \Phi_{0,CLIP} e^{-\alpha_{CLIP} z}. \quad (S33)$$

Suppose that the curing dose D_c is received by an infinitesimally small region of resin being drawn continuously upwards at a velocity V_{CLIP} once it has traveled a distance L_c upwards from the top of the dead zone (while in the dead zone, no curing can begin). Then:

$$\int_0^{D_c} dD = \alpha_{CLIP} \Phi_{0,CLIP} \int_0^{L_c/V_{CLIP}} e^{-\alpha_{CLIP} z} dt \quad (S34)$$

where $t = 0$ at the moment the material exits the dead zone. Substituting $z = h_d + V_{CLIP}t$:

$$\int_0^{D_c} dD = \alpha_{CLIP} \Phi_{0,CLIP} \int_0^{L_c/V_{CLIP}} e^{-\alpha_{CLIP}(h_d + V_{CLIP}t)} dt \quad (S35)$$

from which:

$$V_{ill,CLIP} = \frac{\Phi_{0,CLIP} e^{-\alpha_{CLIP} h_d}}{D_c} (1 - e^{-\alpha_{CLIP} L_c}). \quad (S36)$$

By setting the derivative of (S36) with respect to α_{CLIP} to zero and solving for the optimum α_{CLIP}^* , we find that the maximal printing speed occurs when:

$$\alpha_{CLIP}^* L_c = \ln\left(\frac{L_c}{h_d} + 1\right). \quad (S37)$$

As the ratio of dead zone thickness to slicing thickness, h_d/L_c , increases, the optimal dimensionless absorption coefficient, $\alpha_{CLIP}^* L_c$, falls (Fig. S13B). Realistic values of h_d lie between 20 μm and 100 μm (11), which are actually comparable in magnitude to commonly desired printed layer thicknesses, so we can expect h_d/L_c to lie between 0.1 and 1 in practical cases. Thus, from (S37) and Fig. S13B, setting $\alpha_{CLIP} \approx 1/L_c$ would appear to offer reasonable speed and layer resolution.

(c) Exposure time in CAL

In CAL, the minimum necessary time for curing can be modeled by considering the photon absorption density history at a general point P in the rotating container of photosensitive material (Fig. S14A). This point lies a radial distance c from the center of the rotating container with radius R . Assuming negligible absorption in the passive, index-matched material surrounding the rotating container, the propagation distance w traveled through absorbing material by photons reaching point P varies with rotation angle θ in the following way:

$$w = \sqrt{R^2 - c^2 \sin^2 \theta} - c \cos \theta. \quad (S38)$$

Point P cures at a time $T_{C,CAL}$, when the cumulative photon absorption per unit volume reaches the curing dose D_c . Assuming that the time for one rotation is considerably less than $T_{C,CAL}$ —an operating approach that has been found to minimize patterning distortions arising from temporal refractive index changes—curing occurs when:

$$D_c = \frac{T_{C,CAL}}{2\pi} \int_0^{2\pi} B_{CAL} d\theta. \quad (S39)$$

Rearranging and substituting the photon absorption rate, $B_{CAL} = \alpha_{CAL}\Phi_{0,CAL}e^{-\alpha_{CAL}w}$:

$$T_{C,CAL} = \frac{2\pi D_c}{\int_0^{2\pi} B_{CAL} d\theta} = \left(\frac{D_c}{\Phi_{0,CAL}} \right) \frac{2\pi}{\alpha_{CAL} \int_0^{2\pi} e^{-\alpha_{CAL}w} d\theta}. \quad (\text{S40})$$

The (numerically evaluated) dimensionless print time $T_{C,CAL}\Phi_{0,CAL}D_c^{-1}R^{-1}$ is shown in Fig. S14B against the relevant dimensionless absorption parameter $\alpha_{CAL}R$ for values of the dimensionless radial position c/R spanning from 0 (the point at the center of the rotating volume) to 1 (points at the edge of the rotating volume). It is seen that the case of $c/R = 0$ constrains the minimum achievable print time and that the minimum print time $T_{C,CAL,\min}$ occurs when $\alpha_{CAL}R = 1$. This finding has significant implications for the formulation of photosensitive materials for CAL.

We can evaluate $T_{C,CAL,\min}$ by setting $w = R$ and $\alpha_{CAL}R = 1$, yielding:

$$T_{C,CAL,\min} = \left(\frac{D_c}{\Phi_{0,CAL}} \right) \frac{2\pi}{\frac{1}{R} \int_0^{2\pi} e^{-1} d\theta} = \left(\frac{D_c}{\Phi_{0,CAL}} \right) eR. \quad (\text{S41})$$

S19. Hydrodynamic model for inter-layer retraction loads in SLA

The printing speeds of PSL and CLIP (but not of CAL) may also be limited by hydrodynamic stresses arising between the transparent window and the printed part as it translates in the z direction. As the component is drawn upwards, liquid resin needs to flow into the gap(s) between the part and the window. A reasonable model for the relationship between printed geometries, hydrodynamic loads, and z velocity comes from using the lubrication approximation (41) to model the flow of material into this gap.

Suppose that the part being printed, as viewed through the printing window, consists of multiple circular features with radii $c_0 \gg h_d + L$ (for CLIP, $c_0 \gg h_d + L_c$) that are sufficiently far apart that liquid resin is readily supplied to their outer edges. Therefore, all loads acting between the part and the window can be considered to be transmitted through thin cylindrical regions (disks) of uncured material between the features and the window (Fig. S12C, Fig. S13A).

Where the instantaneous total height of the gap is h , and assuming the uncured resin is modeled as Newtonian with dynamic viscosity η , the relationship between the rate of change of h and the pressure $p(c)$ in the gap at radial distance c from the center of the feature is:

$$p(c) - p_c = -\frac{3\eta c_0^2}{h^3} \left(\frac{dh}{dt} \right) \left[1 - \left(\frac{c}{c_0} \right)^2 \right]. \quad (\text{S42})$$

Here, p_c is the pressure in the surrounding fluid. The average pressure p_0 across the disk, relative to the surrounding material, is thus:

$$p_0 = \left(\frac{1}{\pi c_0^2} \right) \int_{c=0}^{c=c_0} p(c) 2\pi c \, dc = -\frac{3\eta c_0^2}{h^3} \left(\frac{2}{c_0^2} \right) \left(\frac{dh}{dt} \right) \left[\frac{c^2}{2} - \frac{c^4}{4c_0^2} \right]_{0}^{c_0} = -\frac{3\eta c_0^2}{h^3} \left(\frac{dh}{dt} \right). \quad (\text{S43})$$

(a) *Hydrodynamic stresses in PSL*

In PSL, the gap can be considered to begin the retraction step with a thickness equal to the dead zone thickness h_d (the layer that remains oxygen-inhibited) and to finish it with a thickness equal to $h_d + L$, where L is the layer thickness (Fig. S12C).

We suppose that the most negative allowable average pressure on a given feature is $p_{0,limit}$ (we use a positive-compressive sign convention for p_0). This limit might be determined by the strength of partially cured material or by a desire to limit elastic distortions of the transparent window. The shortest achievable value of the time for retraction $t_{hyd,PSL}$ is given by rearranging and integrating (S43) as:

$$t_{hyd,PSL} = \frac{3\eta c_0^2}{2p_{0,limit}} \left[\frac{1}{(h_d + L)^2} - \frac{1}{h_d^2} \right]. \quad (\text{S44})$$

In a case where the hydrodynamic stresses dominate the printing speed, the maximum velocity, $V_{hyd,PSL}$, therefore approaches $L/t_{hyd,PSL}$:

$$V_{hyd,PSL} = \frac{2p_{0,limit}L}{3\eta c_0^2} \left[\frac{1}{(h_d + L)^2} - \frac{1}{h_d^2} \right]^{-1}. \quad (\text{S45})$$

(b) *Hydrodynamic stresses in CLIP*

In CLIP, where the retraction and illumination of the part are continuous and concurrent, and solidification of the resin occurs a distance $h_d + L_c$ from the transparent window, the pressure distribution in the gap can be regarded as steady over time (Fig. S13A). Substituting $h = h_d + L_c$ and rearranging (S43), the hydrodynamic limit on the maximum achievable printing velocity, $V_{hyd,CLIP}$, is then:

$$V_{hyd,CLIP} = -\frac{(h_d + L_c)^3}{3\eta c_0^2} p_{0,limit}. \quad (\text{S46})$$

This model is likely, if anything, to over-estimate $V_{hyd,CLIP}$, because at distances between h_d and $h_d + L_c$ from the transparent window, crosslinking will have begun and the viscosity will therefore have begun to increase relative to its uncured state.

From both (S44) and (S46), an inverse-square relationship is apparent between feature size c_0 and the hydrodynamic limit on printing speed. For printing a given volume of material in a PSL or CLIP process, then, it will be preferable to divide the material into the smallest possible segments, creating porous or cellular structures as opposed to solid monoliths. While such structures might actually be desirable in some components (42), there is no inherent need for these design constraints in CAL because of the absence of the hydrodynamic considerations described above.

S20. Overall print speed comparison

(a) *Integration of models*

In Table S1, we show how the illumination-based and hydrodynamic limitations on printing speed interact in the three processes. For PSL, because illumination and retraction steps occur alternately, the overall printing speed depends on both of these speeds, as shown. For CLIP, however, since illumination and retraction are concurrent, printing speed is dictated by the lower of the illumination-limited and hydrodynamically-limited speeds.

In CAL, only the illumination time is relevant to the achievable printing speed because there is no thin film of uncured resin to impose a hydrodynamic limit. Because all points in the CAL printing volume are exposed simultaneously, there is no single ‘direction’ in which a printing velocity can be defined, so to provide a speed comparison with PSL and CLIP we consider the case of a cubic target printing volume of side-length H . The assumption of a cubic print volume (as opposed to one with a larger aspect ratio) is consistent with many commercial additive manufacturing tools today and with the ability to produce a wide range of useful structures. To print a volume of $H \times H \times H$ in CAL, the circle of radius $2R$ that is defined by the edge of the photosensitive material container and is capable of being illuminated by the projector in the $r-t$ plane must circumscribe an $H \times H$ region, implying that $R = H/\sqrt{2}$.

Meanwhile, for a projector of a given output power, the comparable incident photon flux in CAL, $\Phi_{0,CAL}$, is equal to $\left(\frac{H}{2R}\right)\Phi_{0,PSL} = \Phi_{0,PSL}/\sqrt{2}$ because the projector must be able to address points across a width of $2R = \sqrt{2}H$ and intensity is inversely proportional to exposed area. (In the z direction of the CAL setup, which is parallel to the axis of rotation, the exposed region remains H tall in this model.)

Taking $R = H/\sqrt{2}$, and $\Phi_{0,CAL} = \frac{\Phi_{0,PSL}}{\sqrt{2}} = \frac{\Phi_{0,CLIP}}{\sqrt{2}}$ for a comparable print volume in the two processes results (from (S41)) in an effective V_{CAL} of:

$$V_{CAL} = \frac{H}{T_{c,CAL,\min}} = \left(\frac{\Phi_{0,PSL}}{D_c}\right)e^{-1}. \quad (\text{S47})$$

(b) *Evaluation of models for realistic parameters*

The question of which printing process is faster in particular circumstances depends on a large number of parameters. To enable a realistic comparison, we adopt the ranges in Table S2.

For the dead zone thickness, h_d , we adopt the following model, after Tumbleston (II) :

$$h_d = C \left(\frac{\Phi_{0,PSL} \alpha}{D_c} \right)^{-0.5} \quad (\text{S48})$$

where $C = 30 \times 10^{-6} \text{ m s}^{-0.5}$. In this work we assume $\alpha = \alpha_{PI}$ (see note in Table S2). Curing dose D_c is assumed to take the value for D_{c0} extracted from our BPAGDA/PEGDA resin as described in Section S6.

(c) *Comparison between CAL and PSL speeds*

In Fig. S15 we evaluate the overall achievable PSL printing speed (V in Table S1) across the parameter space identified in Table S2. Each sub-plot of Fig. S15 shows V_{PSL} against layer thickness, L , for a particular combination of Φ_0 and α and a range of c_0 and $p_{0,limit}$. On each sub-plot, we also show the effective CAL printing speed, V_{CAL} , for that combination of Φ_0 and α , assuming that the optimal absorption coefficient for CAL is being used in each case: $\alpha R = 1$ (see Section S18 for derivation).

As either Φ_0 or α increases, there are two competing effects on V_{PSL} : the time for curing reduces because of more intense absorption of photons, but the dead zone thickness h_d also decreases because of the more rapid consumption of oxygen. The decrease of h_d raises the time needed for inter-layer retraction because the fluid thickness is smaller at the beginning of retraction. There may also be a minimum practicable value of h_d (e.g. $h_d \approx 20 \mu\text{m}$ as identified by Tumbleston (11)) because of the possibility of cured resin sticking to the transparent window. In Fig. S15, cases where $h_d < 20 \mu\text{m}$ are shown with black-shaded symbols while those with larger h_d have open symbols.

Moreover, as feature size c_0 grows or the magnitude of $p_{0,limit}$ reduces, the relative impact of the hydrodynamic stresses increases, reducing V_{PSL} . For the smallest values of c_0 and largest values of $p_{0,limit}$, the hydrodynamic role is at its smallest, and V_{PSL} approaches V_{CAL} most closely. However, for all cases considered, $V_{PSL} < V_{CAL}$, favoring CAL. As derived in Section S18, the location of maximal V_{PSL} is seen to tend towards $\alpha L = 1$ for small c_0 and large-magnitude $p_{0,limit}$. The ratio by which CAL is faster than PSL is at least 1.11, but reaches several orders of magnitude where the hydrodynamic role is substantial or αL is far from 1. From Table S1, the speed ratio when hydrodynamic effects are negligible tends towards:

$$\frac{V_{CAL,max}}{V_{PSL,max}} = \frac{V_{ill,CAL}}{V_{ill,PSL}} = 1 + \frac{h_d}{L}. \quad (\text{S49})$$

(d) *Comparison between CAL and CLIP speeds*

In Fig. S16 we evaluate the overall achievable CLIP printing speed (V in Table S1) across the parameter space identified in Table S2. Using the same format as the PSL analysis above, each sub-plot of Fig. S16 shows V_{CLIP} against slicing thickness, L_c , for a particular combination of Φ_0 and α and a range of c_0 and $p_{0,limit}$. On each sub-plot, we also show the effective CAL printing speed, V_{CAL} , as we did in Fig. S15.

CLIP behaves rather differently from PSL in that for a given combination of Φ_0 and α in a purely illumination-dominated case where $h_d \ll L_c$, V_{CLIP} increases monotonically with L_c rather than showing an optimum. In practice, as discussed above, one would not simply choose an arbitrarily large L_c to maximize V_{CLIP} because z resolution also has to be considered. From (S36) and (S47), it follows that the speed ratio in the illumination-dominated limit is:

$$\frac{V_{\text{CAL},\max}}{V_{\text{CLIP},\max}} = \frac{e^{\alpha_{\text{CLIP}} h_d - 1}}{1 - e^{-\alpha_{\text{CLIP}} L_c}}. \quad (\text{S50})$$

For $h_d \rightarrow 0$ and $\alpha_{\text{CLIP}} L_c < -\ln(1 - e^{-1}) = 0.46$, CAL would be faster than CLIP. For $h_d \rightarrow 0$ and $\alpha_{\text{CLIP}} L_c = 1$ (implying reasonable CLIP z -resolution), CLIP would be a factor of $e - 1$ faster than CAL. For $h_d \rightarrow 0$ and $\alpha_{\text{CLIP}} L_c \rightarrow \infty$, CLIP tends to being a factor of e faster than CAL. These limits, however, correspond to the absolute maximum speeds achievable with CLIP. As Fig. S16 shows, as c_0 grows or $p_{0,\text{limit}}$ shrinks in magnitude, the hydrodynamic factor becomes appreciable and then dominant, pulling V_{CLIP} down to as much as four orders of magnitude smaller than V_{CAL} for the highest- Φ_0 , highest- α case modeled (Fig. S16F).

Moreover, as Φ_0 and α increase, h_d reduces, eventually reaching the lower practical limit (11). The black-shaded symbols in Fig. S16E–F indicate that $h_d < 20 \mu\text{m}$; these cases may be impracticable, further favoring CAL.

What this analysis illustrates is that as steps are taken to speed up the printing process by using brighter illumination or more concentrated photoinitiator, CAL's speed becomes increasingly attractive. For an illumination intensity of 87 W m^{-2} , an effective printing speed of $\sim 5.4 \text{ m/hour}$ is predicted for CAL under the assumed conditions.

Of course, CAL's potentially very high printing speed is advantageous only when it can also deliver the requisite spatial resolution. Our analysis in Sections S16 and S17 provides a framework for determining this resolution, and the discussion in the context of the present experiments shows that sub-mm feature sizes are readily achievable.

(e) Role of passive dye in PSL and CLIP

It should be noted that all of the above analysis is done without any passive dye in the resin, and so corresponds to the highest conceivable PSL or CLIP printing speeds for a given set of operating parameters. In typical layer-by-layer systems, however, it is often necessary to add a considerable amount of passive dye to the photosensitive material. This dye may be needed to achieve a high enough absorption coefficient to absorb illumination within the desired layer, while maintaining a practicably large dead-zone thickness. Then, the total absorption coefficient α is given by:

$$\alpha = \alpha_{PI} + \alpha_{dye} \quad (\text{S51})$$

where α_{PI} is the absorption coefficient due to the photoinitiator and α_{dye} is that due to the passive dye. The addition of dye raises D_c by a factor α/α_{PI} relative to a case without dye, because a fraction α_{dye}/α of incident photons is passively absorbed and cannot contribute to curing. The dye thus slows down the PSL/CLIP process for a given projector power.

In CAL, on the other hand, the optimal absorption coefficient is a factor of $\sim R/L$ lower than for PSL/CLIP. Since $R \gg L$, it is feasible to omit a passive dye. Therefore, realistic D_c values for CAL resins can be expected to be much smaller than for PSL/CLIP resins, resulting in a further print speed advantage for CAL over PSL/CLIP over and above those already quantified.

(f) Postprocessing considerations

In addition to the illumination and hydrodynamic contributions to printing time, post-processing time must be considered. Postprocessing usually involves rinsing away uncured resin and possibly completing a flood exposure or baking step to bring curing to completion. The time needed for resin rinsing and flood exposure in CAL is expected to be comparable to that in layer-by-layer techniques. However, CAL has the advantage of not requiring solid supports to be removed, a process whose duration depends on user skill but, by being eliminated, will significantly shorten post-processing time.

S21. Relationship between printing speed and spatial resolution

Here we model how sampling requirements, photopolymer kinetics and projection hardware capabilities interact to determine the overall relationship between printing speed and resolution of a CAL system.

In Section S15, we noted that the number of angular samples required to avoid aliasing during reconstruction is $N_\theta \geq \frac{\pi}{2} N_r$, where $N_r = 2R/x$, x is the radial sampling period and R is the radius of the geometry. We assume in this section that the projected pixel size d equals the radial sampling period, meaning $d = x$, and that the geometry fills the printing volume so that R is also the radius of the container. Meanwhile, from Equation (S41) the minimum illumination time for resin solidification in CAL is:

$$T_{C,CAL,min} = \left(\frac{D_c}{\Phi_{0,CAL}} \right) eR. \quad (S52)$$

To be able to deliver the minimum number of projections N_θ before the curing dose D_c is reached, the refresh rate of the projector f_p needs to be high enough to deliver all the projections within $T_{C,CAL,min}$:

$$f_p \geq \frac{N_\theta}{T_{C,CAL,min}} = \frac{\pi \Phi_{0,CAL}}{d D_c e} \quad (S53)$$

It will be helpful to evaluate printing capabilities for a given absolute optical output power, to enable selection of a projector model. To this end, $\Phi_{0,CAL}$ can be expressed in terms of the useful optical output power of the projector's illumination source $P_{optical}$, the photon energy E_{photon} , and R , assuming the projector to have a width-to-height aspect ratio of $\sqrt{2}$, as:

$$\Phi_{0,CAL} = \frac{P_{optical}}{E_{photon} 2\sqrt{2}R^2}. \quad (S54)$$

Rearranging (S53) and substituting from (S54) we have an expression for the minimum sampling period allowable, which can be taken to represent spatial resolution:

$$d \geq \frac{\pi P_{optical}}{E_{photon} 2\sqrt{2}R^2 f_p D_c e}. \quad (\text{S55})$$

Meanwhile the upper limit of the volumetric rate of printing Q is the ratio of accessible print volume (assumed a cube of side length $H = \sqrt{2}R$) to the minimum print time:

$$Q = \frac{H^3}{T_{c,CAL,min}} = \frac{P_{optical}}{E_{photon} D_c e}. \quad (\text{S56})$$

So the maximum volumetric printing rate is simply proportional to the total illumination power available. We visualize contours of Q on a plot of d against R (Fig. S19). An additional constraint is the hardware requirement that there be at least N_r pixels across the width of the pattern generator in the projection system, and this limitation is also plotted on the chart for three common projector resolutions (WXGA, full HD, and 4K).

In addition to this system-level set of constraints, we showed in Section S17 that there may be local pattern- and location-dependent trade-offs between MTF and dose per revolution, which is directly correlated with printing speed.

S22. Gravitational effects and printing without solid support structures

The absence of solid support structures in CAL is possible because the uncured photosensitive material surrounding a printed structure exerts adequate forces to prevent it from sinking. To provide a framework for estimating the likely effects of gravity on partially printed geometries, we model the time-dependent vertical velocity V of a printed sphere of radius R_p in a photosensitive liquid of dynamic viscosity μ . Let g be the gravitational acceleration, ρ_s the mass density of the cured material, and ρ_f that of the uncured fluid. The sphere experiences a net gravitational force of

$$F_g = \frac{4}{3}(\rho_s - \rho_f)g\pi R_p^3 \quad (\text{S57})$$

while the opposing Stokes drag on the sphere is

$$F_s = 6\pi\mu R_p V. \quad (\text{S58})$$

The sphere's vertical velocity can therefore be expressed as:

$$\frac{dV}{dt} = \frac{\rho_s - \rho_f}{\rho_s} g - \frac{9\mu}{2R_p^2 \rho_s} V \quad (\text{S59})$$

which integrates to:

$$V = \frac{2gR_p^2(\rho_s - \rho_f)}{9\mu} \left(1 - e^{-\frac{9\mu t}{2R_p^2\rho_s}}\right) \quad (\text{S60})$$

where solidification is assumed to occur instantaneously at time $t = 0$. The above relationship shows that the time constant for reaching the terminal velocity is $2R_p^2\rho_s/9\mu$.

We assume volume shrinkage of 10% upon curing, which is at the upper end of the typical range for acrylate-based crosslinking (45). We therefore assume a mass density increase of 10%, meaning that $\rho_s = 1.1\rho_f$. We also assume $\rho_f = 1100 \text{ kg/m}^3$ and take $\mu = 5000 \text{ cP} \equiv 5 \text{ Pa s}$, as measured for the BPAGDA/PEGDA mixture used in the present work (see Section S1). With these assumptions, the time constant for a printed component of radius $R_p = 5 \text{ mm}$ to reach terminal velocity is $\sim 1.3 \text{ ms}$, and the final velocity is 1.2 mm/s .

If such sinking velocities were truly realized during printing, we would expect mm-scale geometries to become significantly blurred during the print times of ~ 2 minutes that we have used. In fact, sub-mm features are sharply resolved in CAL. Moreover, we have previously demonstrated successful volumetric printing of mm-scale structures in much *lower* viscosity ($\sim 12 \text{ cP}$) materials with $\lesssim 10 \text{ s}$ print times (9). These observations suggest an additional aspect of the uncured materials' behavior, possibly a small but crucial yield stress not captured by the cone-and-plate rheometry but which holds the partially printed structures in place.

S23. Spinning the print volume: time to steady state

For CAL to operate successfully, all points in the photosensitive material must have an equal angular velocity relative to the projection direction. In principle, either the projector can be rotated around a container of stationary material, or the material container can be rotated relative to a stationary projector. The latter approach is taken in the present work, and it may be considered to offer a simpler apparatus than one with a rotating projector. However, the time taken to 'spin-up' the photosensitive material from rest to a steady angular velocity for printing must be considered.

The spinning up of a body of fluid to a steady state of constant angular velocity — also referred to as the 'rigid body' condition — has been widely studied, and the required time depends on the relationship between the geometry of the container, its angular velocity, and the kinematic viscosity of the fluid. For higher velocities, lower viscosities and larger geometries, the spin-up time is governed by outward radial secondary flows which are caused by centrifugal forces, drive convective mixing, and are described by the Ekman time (46):

$$t_{\text{Ekman}} = Hv^{-0.5}\Omega^{-0.5} \quad (\text{S61})$$

where H is the height of a cylindrical container measured along the rotation axis, v is the kinematic viscosity, and Ω is the rotational velocity. For lower velocities, larger viscosities and smaller geometries, the spin-up time is governed by diffusion of momentum, and the radial diffusion time is given (47) by:

$$t_{\text{Diffusion}} = R^2 \nu^{-1} \quad (\text{S62})$$

For a given condition, the smaller of t_{Ekman} and $t_{\text{Diffusion}}$ can be considered predictive of the spin-up time. In Table S3 below we evaluate these times for three cases:

(A) the present work, taking an angular velocity of 15 °/s and the largest print volume (radius 15 mm) used;

(B) a scaled-up print volume with $R = 0.25$ m but with the same resin properties, angular velocity and projector frame rate as case A;

(C) a scaled-up case with $R = 0.25$ m, but considering the case where, rather than using a conventional video frame rate, f_p , of 25 Hz, a much higher refresh rate of 10 kHz is assumed. This refresh rate is consistent with the maximum available binary image refresh rate of a state-of-the-art micromirror display, and represents one possibility for increasing printing speed. The angular velocity is scaled up in proportion to f_p to maintain comparable angular resolution with cases A and B.

The times are evaluated assuming $H = R\sqrt{2}$, which is consistent with a cubic target print volume circumscribed by the container (see Section S20). We see that in the present work, diffusion of momentum dominates the spin-up process, which is completed in less than 0.1 s. For a larger print volume of $R = 0.25$ m at unchanged angular velocity, the spin-up time is expected to exceed 10 s, yet is still unlikely to dominate the total printing time of ~200 s. The spin-up delay could, however, become problematic at even larger values of R . Increasing rotational velocity would be expected to reduce the spin-up delay by lowering the Ekman time, and could be valuable for very large print volumes.

The rotational Reynolds number, $\Omega R^2 / \nu$, is also shown for context, and indicates that while the present work is comfortably within the laminar flow regime and dominated by viscous forces, inertial forces are likely to be significant in scaled-up systems.

S24. Light focusing, refraction and scattering considerations

The projection computation algorithm presented in this work assumes that all rays emanating from the projector remain parallel, unrefracted, and undiffracted as they pass through the printing volume. The assumption of parallel rays is reasonable in the present work because the depth of focus of the projection system is considerably larger than the diameter of the printing volume. Neglecting refraction and diffraction is reasonable because the majority of the print time is consumed by depletion of the inhibiting oxygen, during which the resin remains largely optically homogeneous. Only towards the very end of the exposure does crosslinking occur, with its associated refractive index increase and the possibility of light refraction and diffraction.

For increased print volumes, however, these assumptions may lose their validity. To address the case of a depth of focus comparable to or smaller than the print diameter, the technique of *optical projection tomography*, introduced by Sharpe *et al.* (48), offers inspiration. Sharpe achieved 3D optical microscopy in a configuration reminiscent of established CT, but using optics with a depth of focus around half that of the sample diameter.

As the print volume increases, the propagation distance through photosensitive medium increases and light scattering may require further modeling and compensation in the computation of projections. Even in the present work, some minor surface striation effects are seen in components printed with BPAGDA/PEGDA, which we attribute to small but cumulative scattering effects. In contrast, the samples printed in GelMA are apparently optically smooth, which we attribute to a smaller refractive index increase upon curing and thus less scattering.

S25. Overprinting algorithm

Here, we describe the theoretical basis for the overprinting procedure and the forward model for light exposure. The arguments are provided for the low-attenuation case with the conventional Radon transform, as implemented in this work. The Radon transform $g(r, \theta) = \widehat{T}_0[f_T]$ expressed in projection space has a 180-degree symmetry given by (where $f_T(\mathbf{r}, z)$ is the target geometry):

$$g(r, \theta + \pi) = g(-r, \theta) \quad (\text{S63})$$

This also applies to the filtered projections: $g_{\text{filt}}(r, \theta) = g(r, \theta) * W(r)$, where $*$ represents radial convolution and $W(r)$ is the Ram-Lak filter. Hence, the reconstruction process (related to the forward model) can be simplified to integration over any 180-degree semicircle, rather than the full 360 degrees:

$$f(\mathbf{r}) = \int_{\theta=0}^{2\pi} g(\mathbf{r} \cdot \hat{\theta}, \theta) d\theta = 2 \int_{\theta=\theta_0}^{\theta_0+\pi} g(\mathbf{r} \cdot \hat{\theta}, \theta) d\theta \quad (\text{S64})$$

where θ_0 is the starting angle for exposure over 180 degrees. Given a printing volume with a convex occlusion, it is always possible to find a semicircle to expose every point, as shown in Fig. 4A of the manuscript. Note that only the x - y cross-section needs to be convex; there can be concavities along the z direction. By linearity of the back-projection operator, these half-space exposures for the different points in the volume can then be combined to produce an exposure recipe. This recipe then provides a good initialization for the iterative inverse problem, accounting for the positivity constraint in the projections as well as the shadowing due to the occlusion, as a function of angle of exposure.

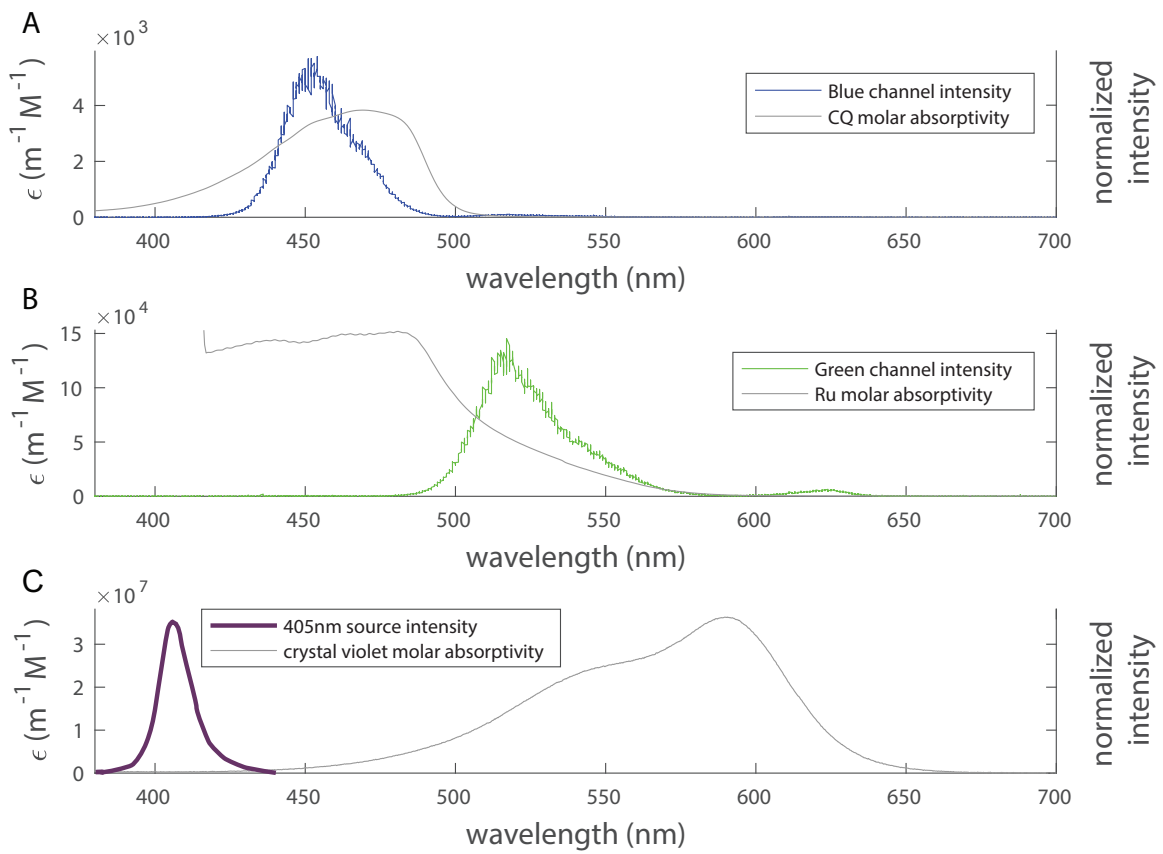


Fig. S1.

Molar absorptivity and illumination spectra of the materials and projector sources used. (A) Absorption spectrum of the BPAGDA/PEGDA resin with CQ photoinitiator, shown together with the intensity spectrum of the blue channel of the DLI Lightcrafter 4500 projector. (B) Absorption spectrum of GelMA hydrogel with Ru photoinitiator, shown together with the intensity spectrum of the green channel of the DLI Lightcrafter 4500 projector. (C) Absorption spectrum of crystal violet (49), together with intensity spectrum of the violet light source of the Wintech Lightcrafter 4500 projector (50).

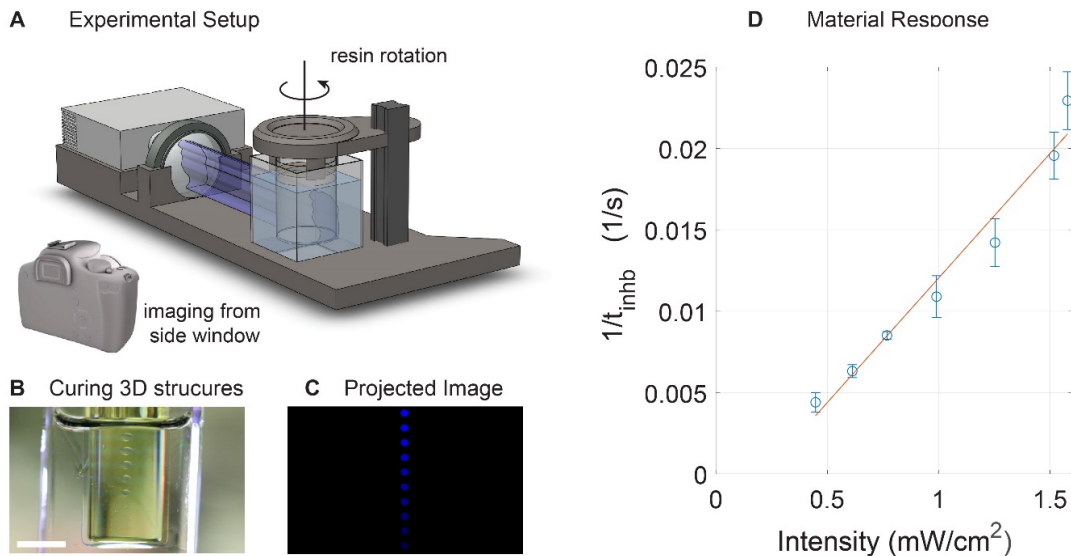


Fig. S2.

Resin response characterization of the 3:1 BPAGDA/PEGDA mixture with CQ photoinitiator. For a range of intensities used from ~0.4–1.6 mW/cm², measured inhibition times support the assumption of linear recording of energy dose. (A) Hardware used for probing the material response. Curing 3D structures in (B) (scale-bar 7.5 mm) are produced from a static image in (C) and rotation of the resin volume. Plot (D) shows data recorded from N=4 trials (N=3 for the highest intensity). Error bars are \pm one sample standard deviation. The red line is the best linear fit to data.

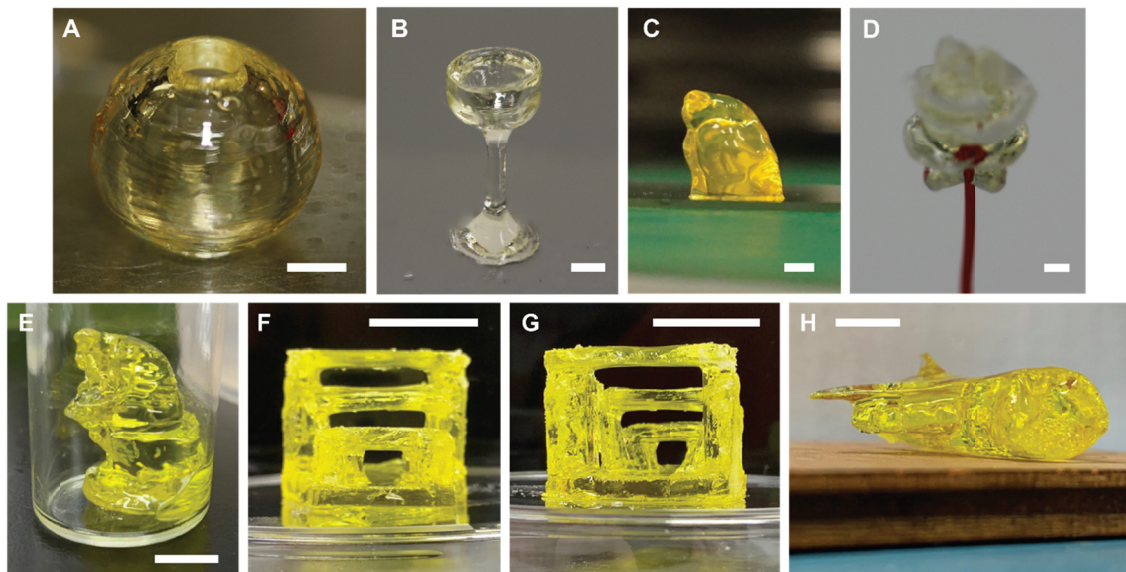


Fig. S3.

Additional geometries printed by CAL. (A) Hollow spherical shell printed in 3:1 BPAGDA/PEGDA. (B) Wine glass (3:1 BPAGDA/PEGDA). (C) The ‘Thinker’ geometry printed in the GelMA hydrogel material. Geometry is distorted *after* removal from uncured material due to gravity and the low stiffness of the hydrogel. (D) Rose geometry over-printed onto a stem (red metal wire and 3:1 BPAGDA/PEGDA). All scale bars (A–D) are 2 mm. (E) ‘Thinker’ printed in 93,000 cP 7:1 BPAGDA/PEGDA (scale bar: 5 mm). (F–G) The bridges of Fig. 2F viewed from different angles (scale bars: 25 mm). (H) Jet plane (3:1 BPAGDA/PEGDA) showing overhanging wing and engines (scale bar: 5 mm).

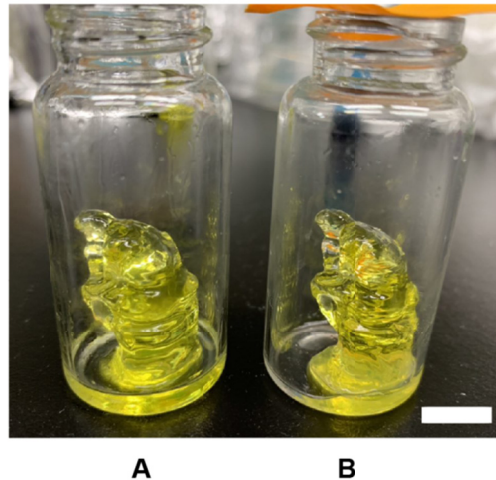


Fig. S4.

Demonstration of regeneration of resin. The image shows a side-by-side comparison of the *Thinker* model printed from (A) fresh resin and (B) uncured resin from the first build after regeneration using the protocol of Section S8. In both cases the projected images and the printing duration of five minutes were identical.

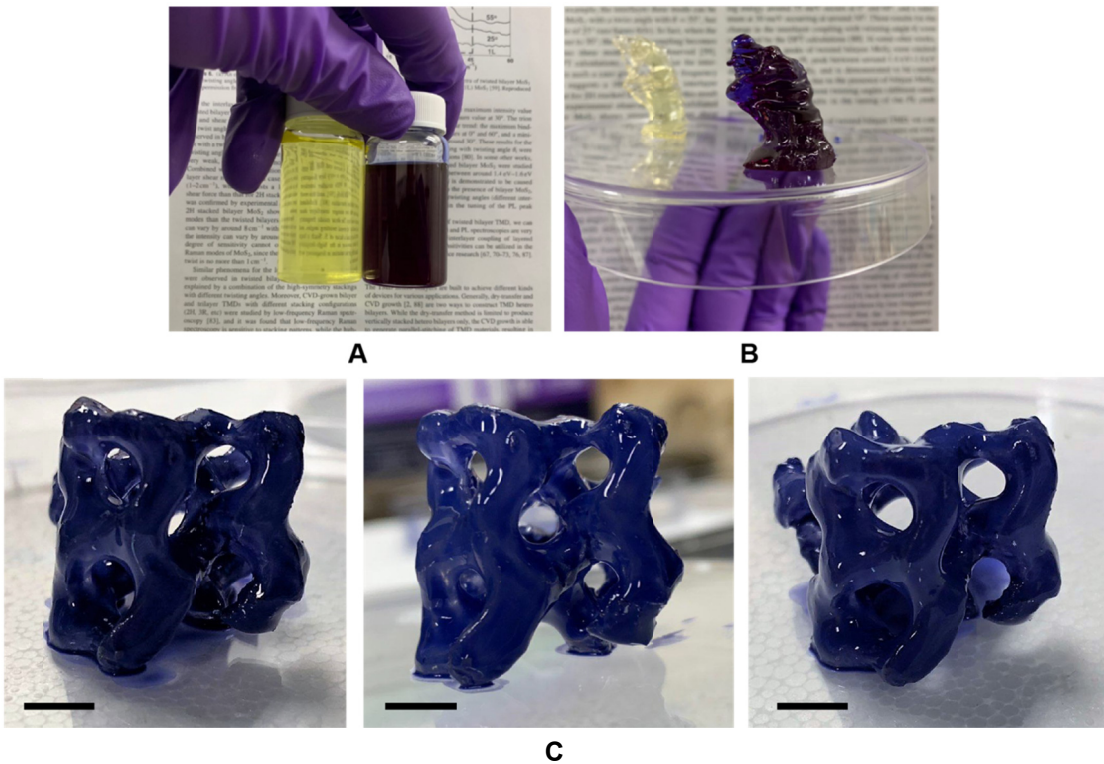


Fig. S5.

Printing opaque parts: (A) vials of 3:1 BPAGDA/PEGDA resin without (left) and with (right) crystal violet; (B) *Thinker* models printed with and without dye using exactly the same exposure conditions; (C) Prototypes of a gyroid geometry printed using the 3:1 BPAGDA/PEGDA mixture with crystal violet (scale bars: 10 mm).

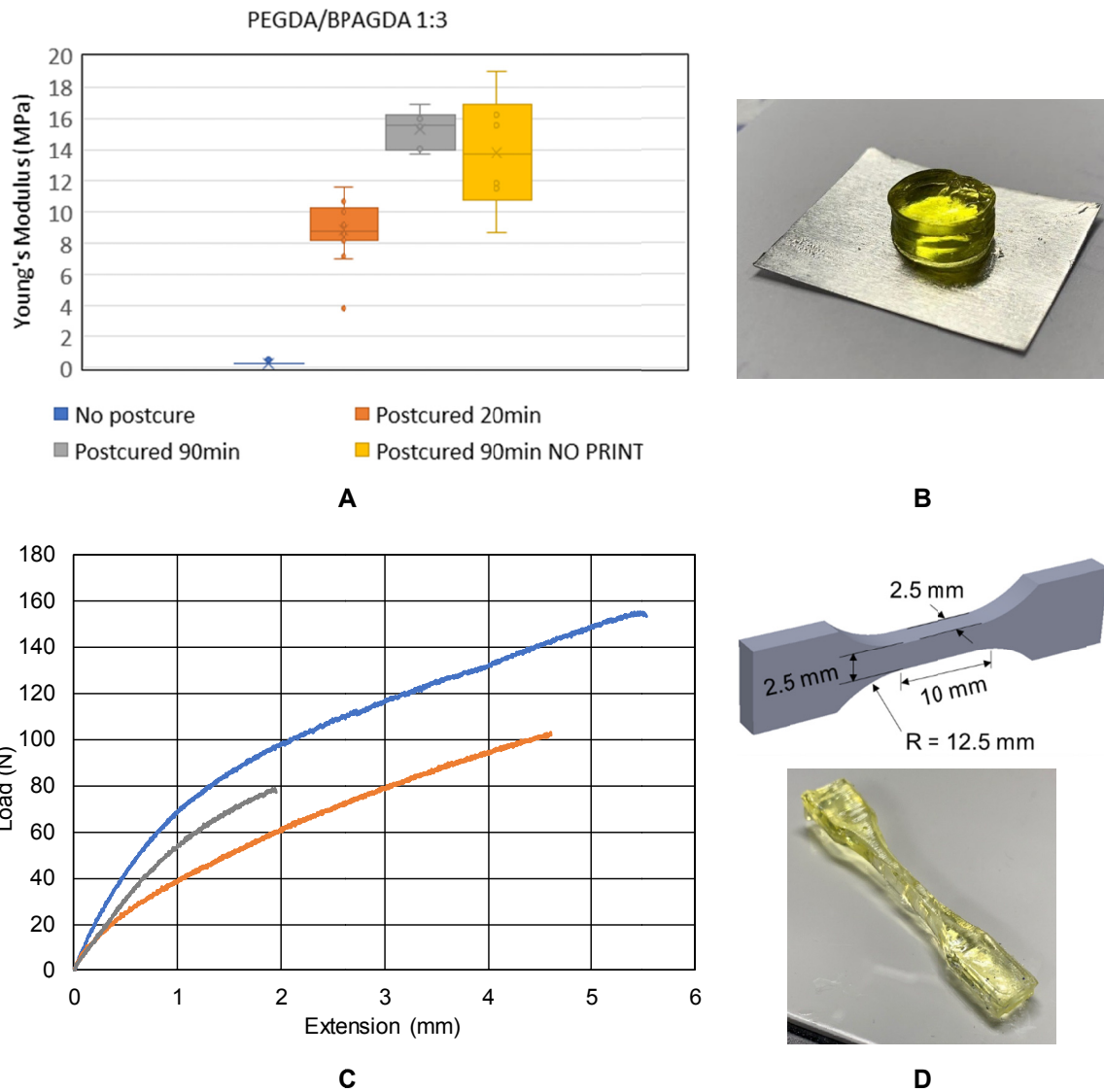


Fig. S6.

Mechanical characterization of 3:1 BPAGDA/PEGDA. (A) Box plots of Young's modulus measured by nanoindentation after CAL exposure without postcure (blue symbols, N=15), CAL exposure followed by 20 min (orange symbols, N=15) and 90 min (gray symbols, N=6) flood postcure in 455 nm light from projector, and 90 min flood exposure without prior CAL printing (yellow symbols, N=6). Boxes encompass the interquartile range. (B) Image of 10 mm-diameter cylindrical sample printed for nanoindentation. (C) Load–extension curves from three independent tensile tests of 3:1 BPAGDA/PEGDA following ASTM D638 Type V standard and post-cured for 45 minutes. (D) Printed dimensions of dogbone samples used, and a photograph of an example dogbone prior to testing.

Image Computation: Projected Gradient Descent

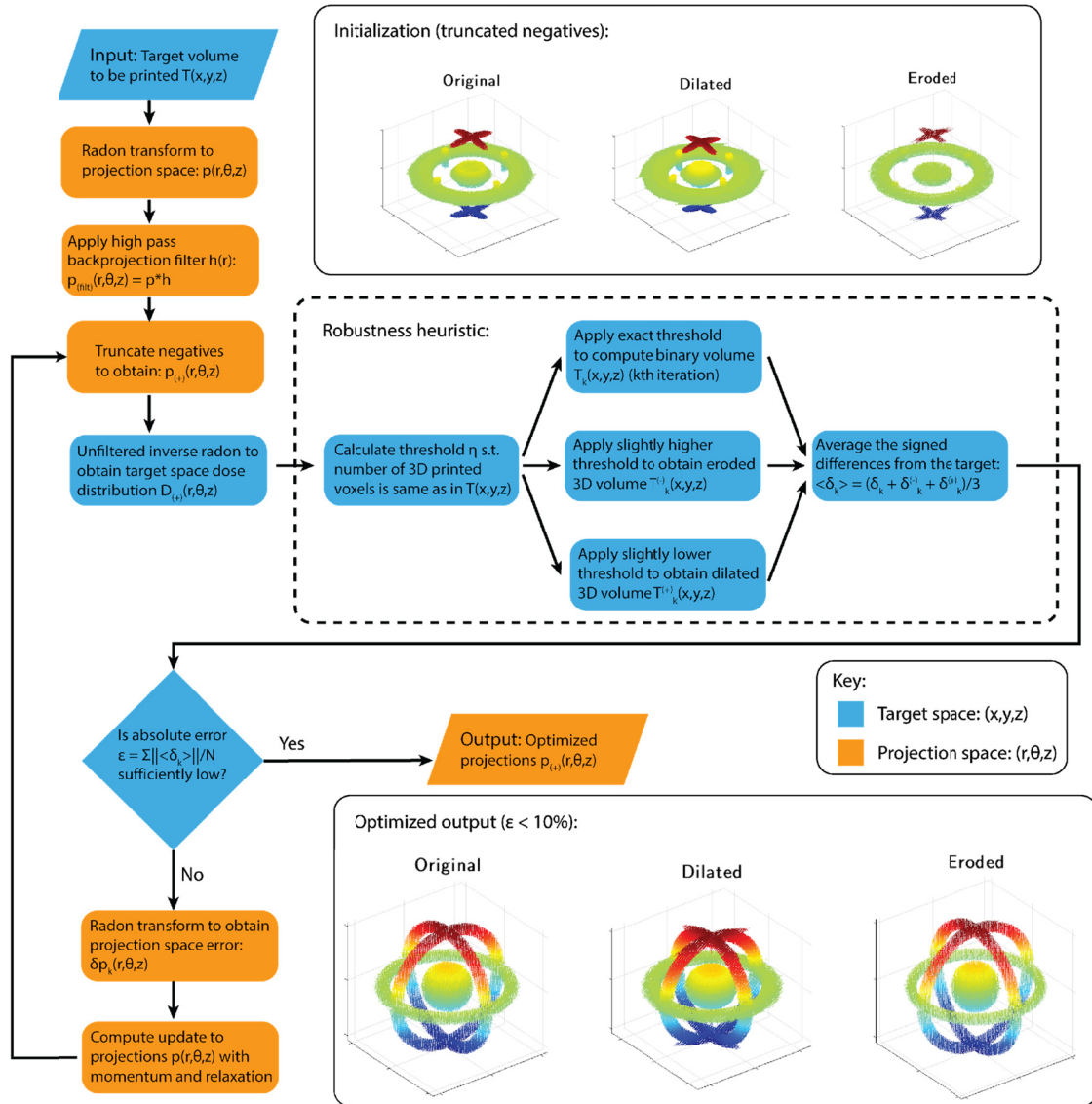


Fig. S7.

CAL algorithm flow chart, corresponding to algorithm pseudocode in Algorithm 1.

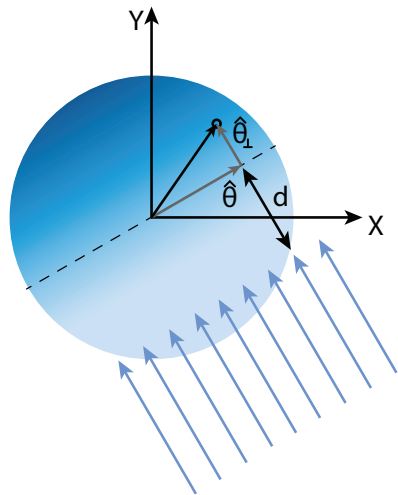


Fig. S8.

Geometry for the exponential Radon transform definition exterior to the print volume.

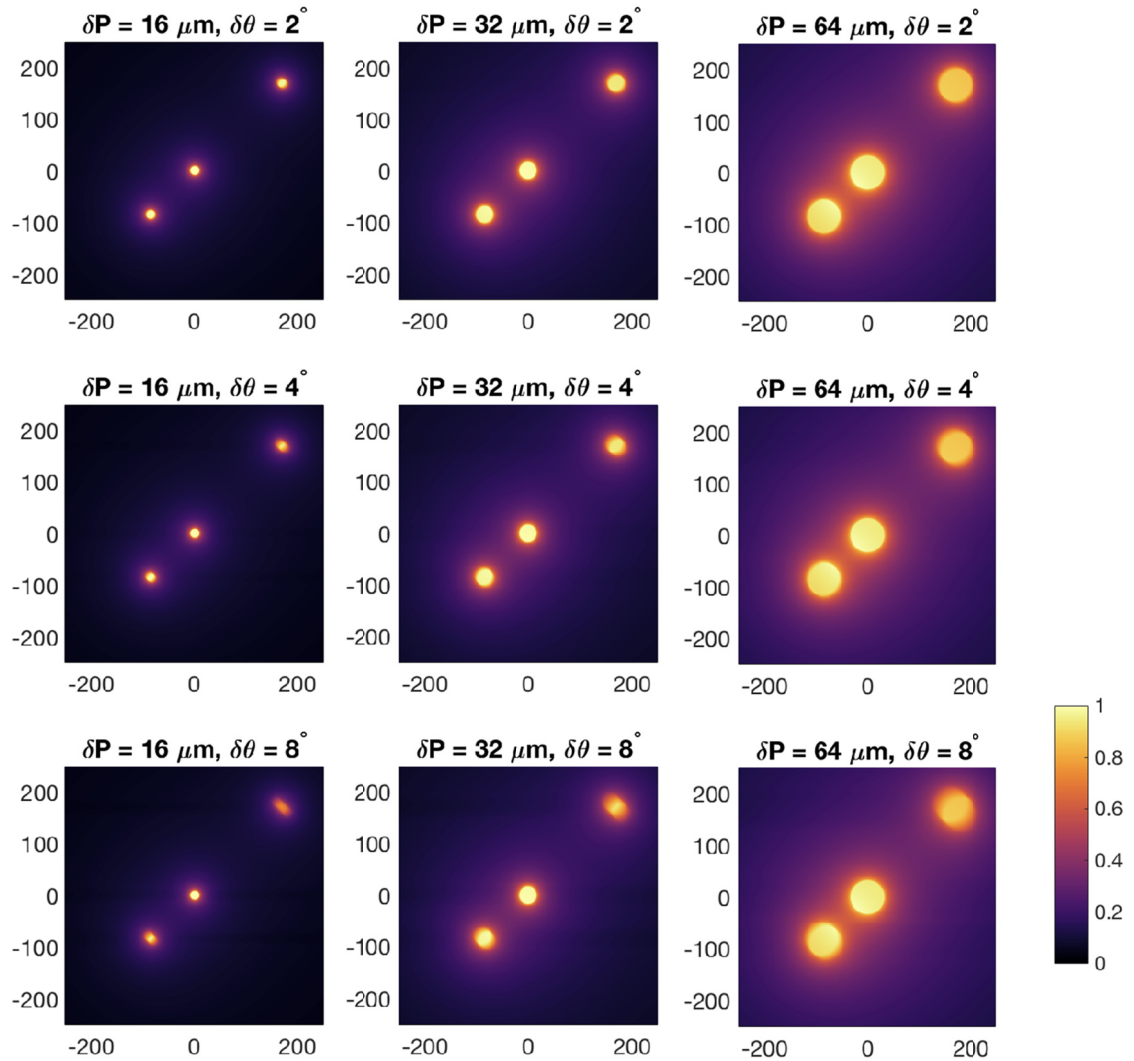


Fig. S9.

Examples of calculated resolution (all axes are spatial coordinates in μm)

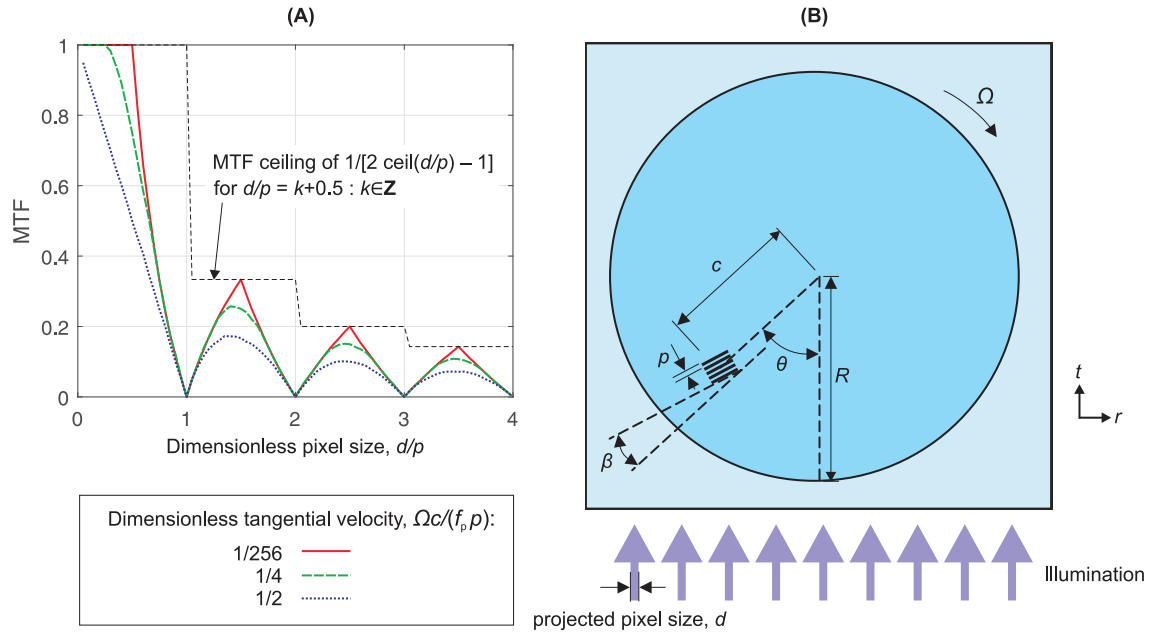


Fig. S10.

(A) Relationships between CAL's modulation transfer function (MTF) and the dimensionless pixel size, d/p , for three different values of dimensionless tangential velocity, $\Omega c/f_p p$. The examples shown here are for a radial position $c/R = 0.1$, optimal absorption coefficient $\alpha = R$, as derived in Section S18, and an azimuthal location $\theta = 0$. For $d < p$, MTF falls with increasing d/p , with larger tangential velocities further degrading MTF. The results also show that smaller secondary peaks in MTF are obtained at $d/p = k + 0.5$ for integer values of k . (B) Nomenclature of the MTF analysis.

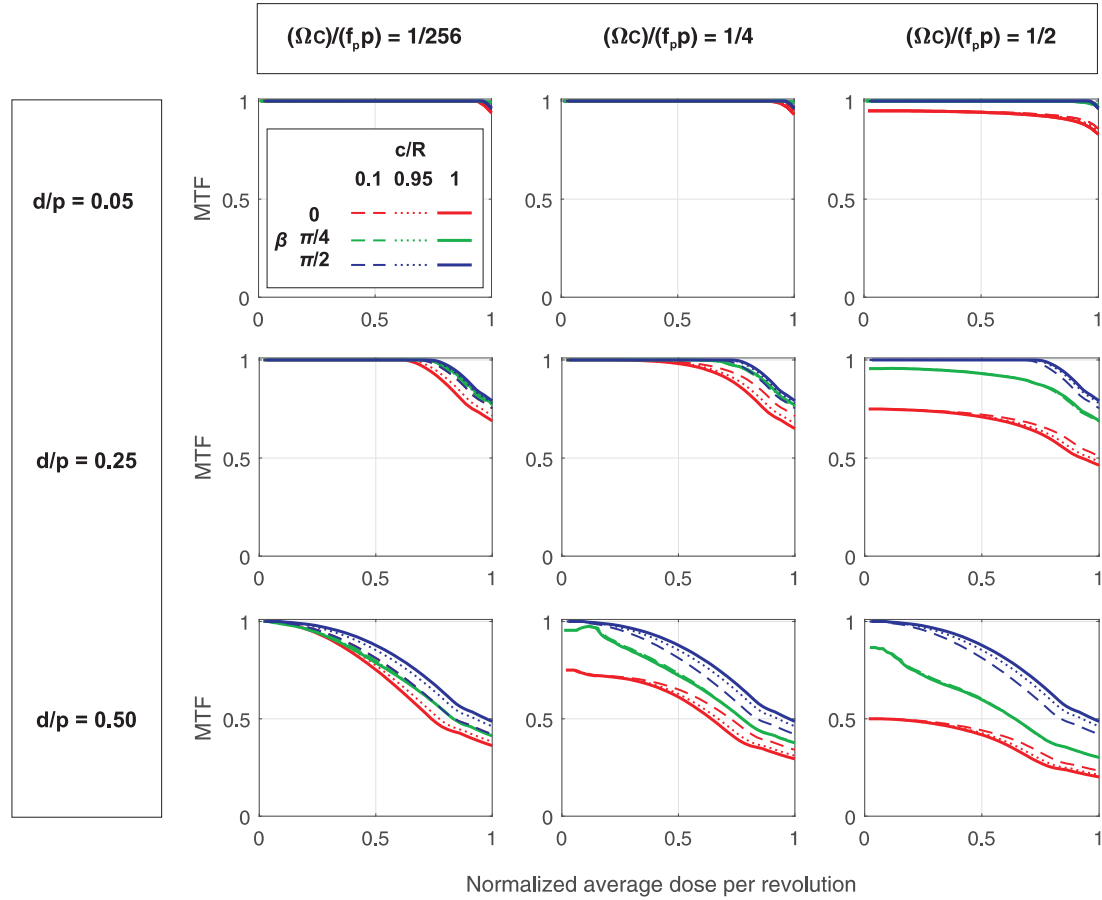


Fig. S11.

Relationships between CAL's modulation transfer function (MTF) and normalized average dose per revolution, for varying dimensionless tangential velocity $\Omega c/f_p p$, dimensionless pixel size d/p , dimensionless radial position c/R , and feature orientation β relative to the radial direction. An optimal absorption coefficient of $\alpha = R$ is assumed. All the curves demonstrate the trade-off between achievable MTF and printing speed, which is positively correlated with normalized dose per revolution. For the case of $\beta = 0$, small radial positions are favored for higher MTF at a given normalized dose, although smaller radial positions will tend to experience lower absolute dosing rates than larger radial positions for a given projector intensity, as shown in Section S18. For $\beta = \pi/2$, however, the *maximal* radial position of $c = R$ is favored for maximal MTF. $\beta = \pi/2$ always offers the highest MTF for given values of the other parameters.

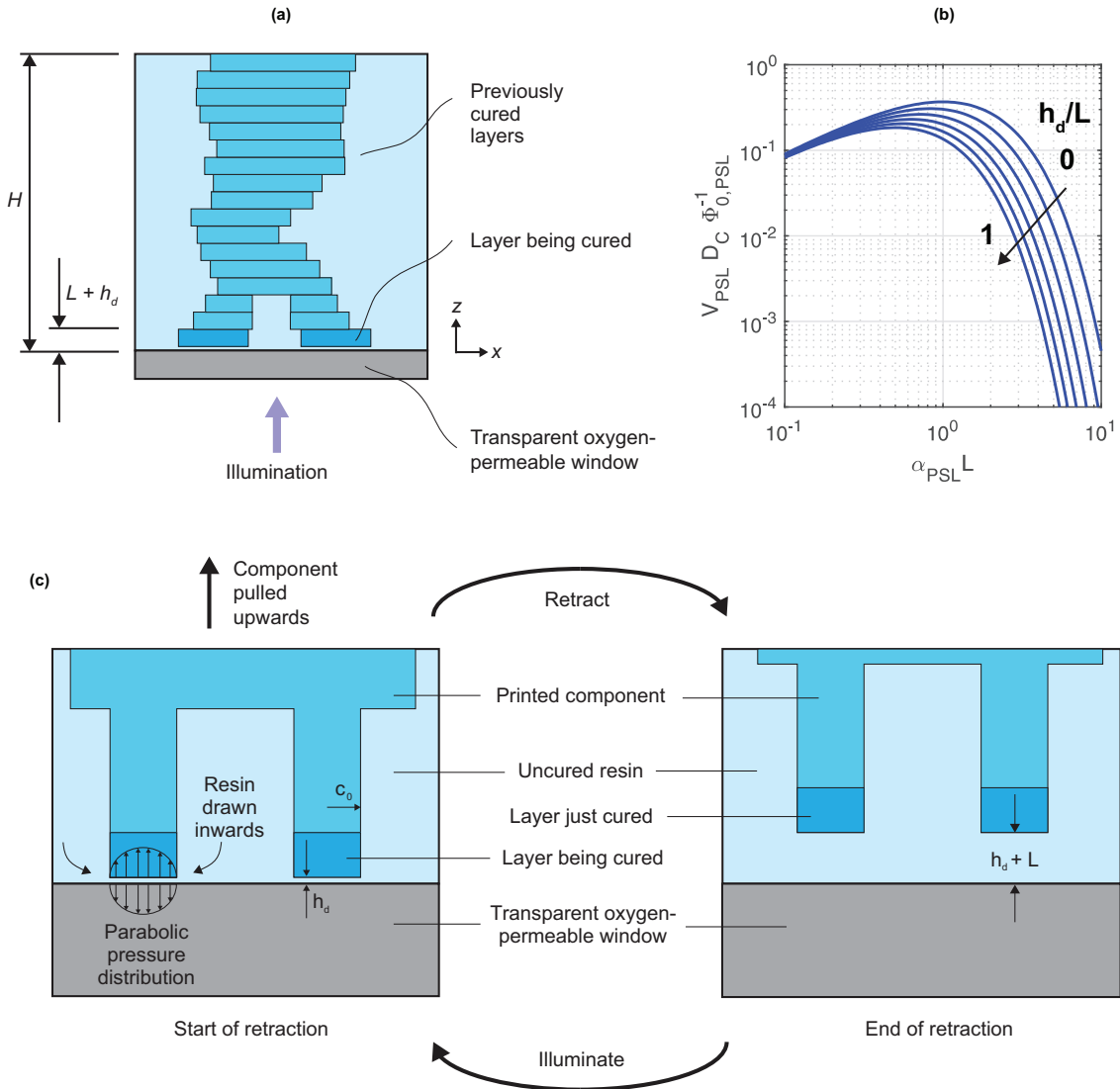


Fig. S12.

Model for PSL. (A) Overall print volume showing component being built from many layers of thickness L . (B) Dimensionless print speed for the illumination time-dominated case. Separate lines correspond to h_d/L increasing from 0 to 1 in steps of 0.2. (C) Close-up of PSL layer-printing: between exposure steps, features of diameter c_0 are pulled upwards to increase the gap between them and the transparent window by one layer thickness, L . The average pressure in each gap is required not to be greater in magnitude than $p_{0,\text{limit}}$. Not to scale: in the model, $c_0 \gg h_d + L$.

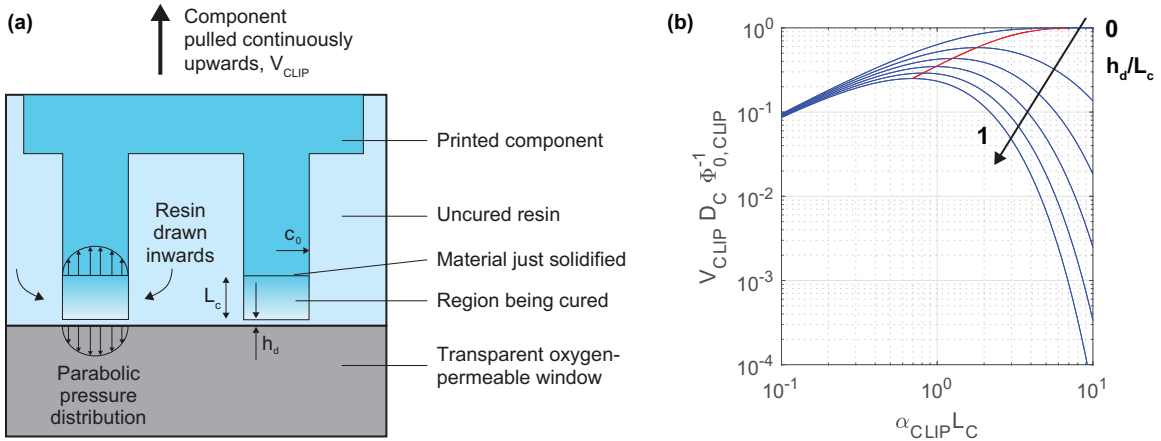


Fig. S13.

Model for CLIP. (A) Close-up of one layer in CLIP case. Not to scale: in the model, $c_0 \gg h_d + L_c$. (B) Dimensionless print speed for the illumination time-dominated case. Separate blue lines correspond to h_d/L_c increasing from 0 to 1 in steps of 0.2. The red line shows the locus of maximal print speed and optimal $\alpha_{CLIP} L_c$ as h_d/L_c increases.

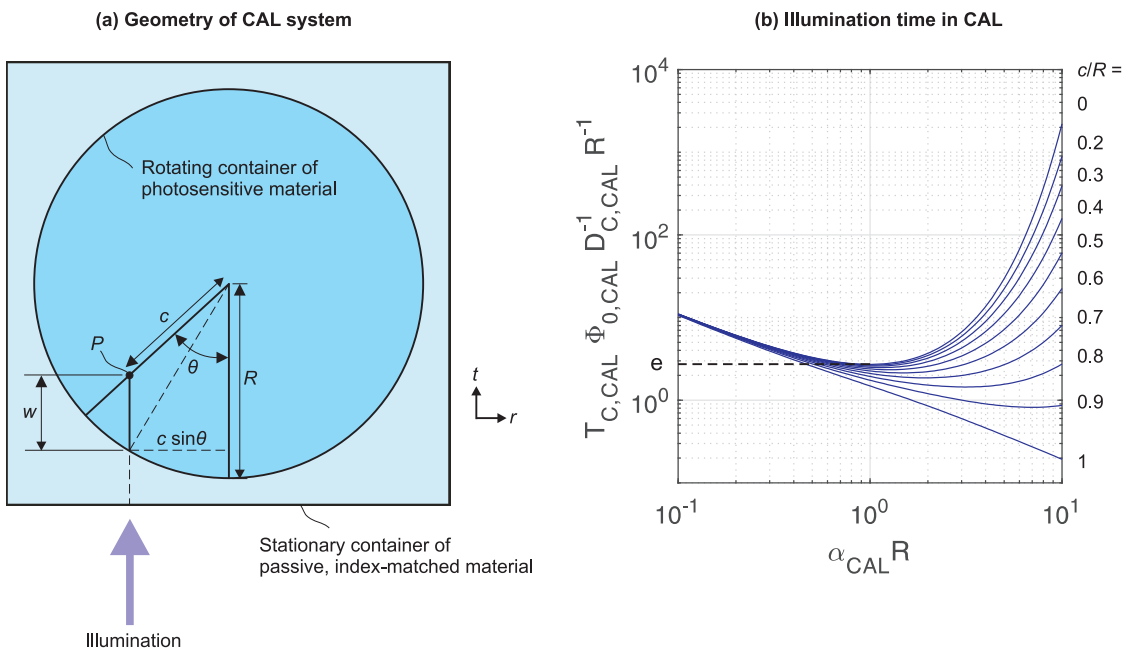


Fig. S14.

CAL system: exposure time model. (A) Nomenclature; (B) Dimensionless exposure time against dimensionless absorption of resin and dimensionless radial position.

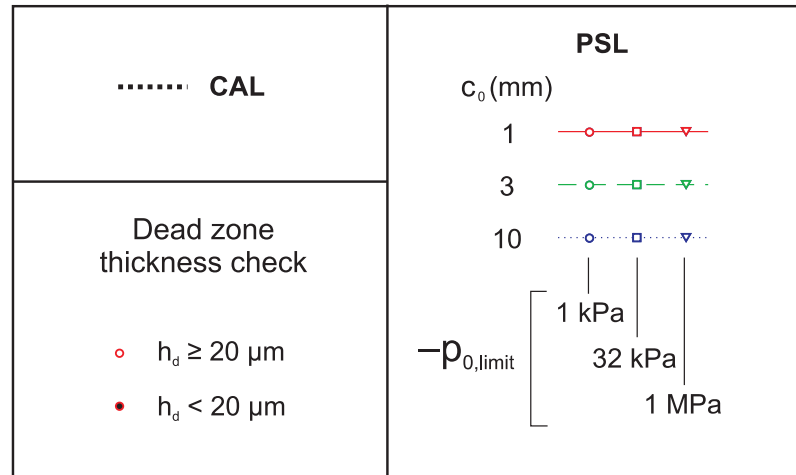
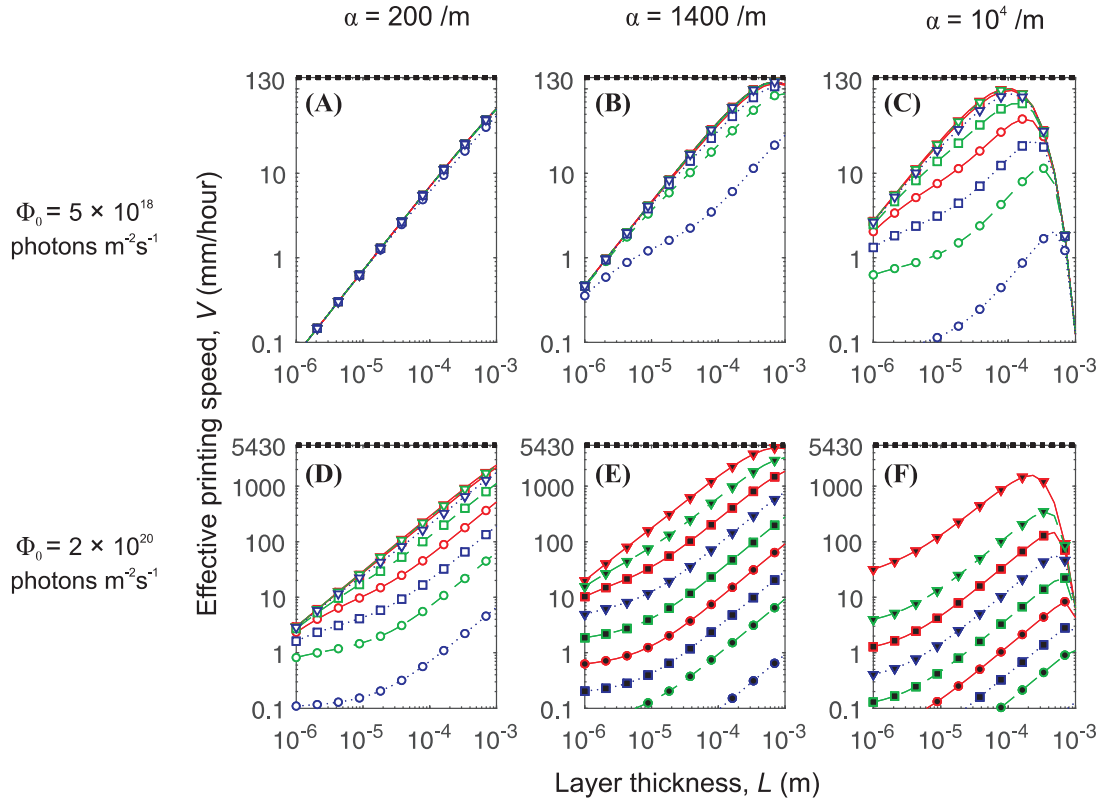


Fig. S15.

Speed comparison: CAL vs PSL. Open symbols indicate that dead zone thickness, $h_d \geq 20 \mu m$. Black-shaded symbols indicate $h_d < 20 \mu m$. This set of curves holds for all values of H considered, although limitations of absolute of projector power may become relevant at large H .

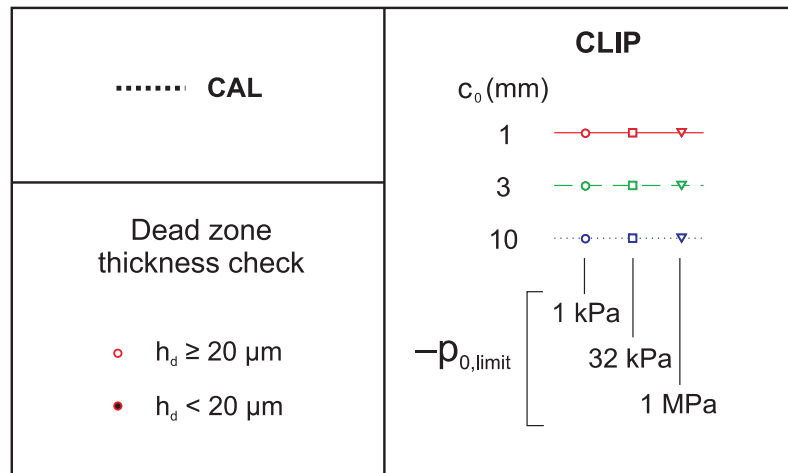
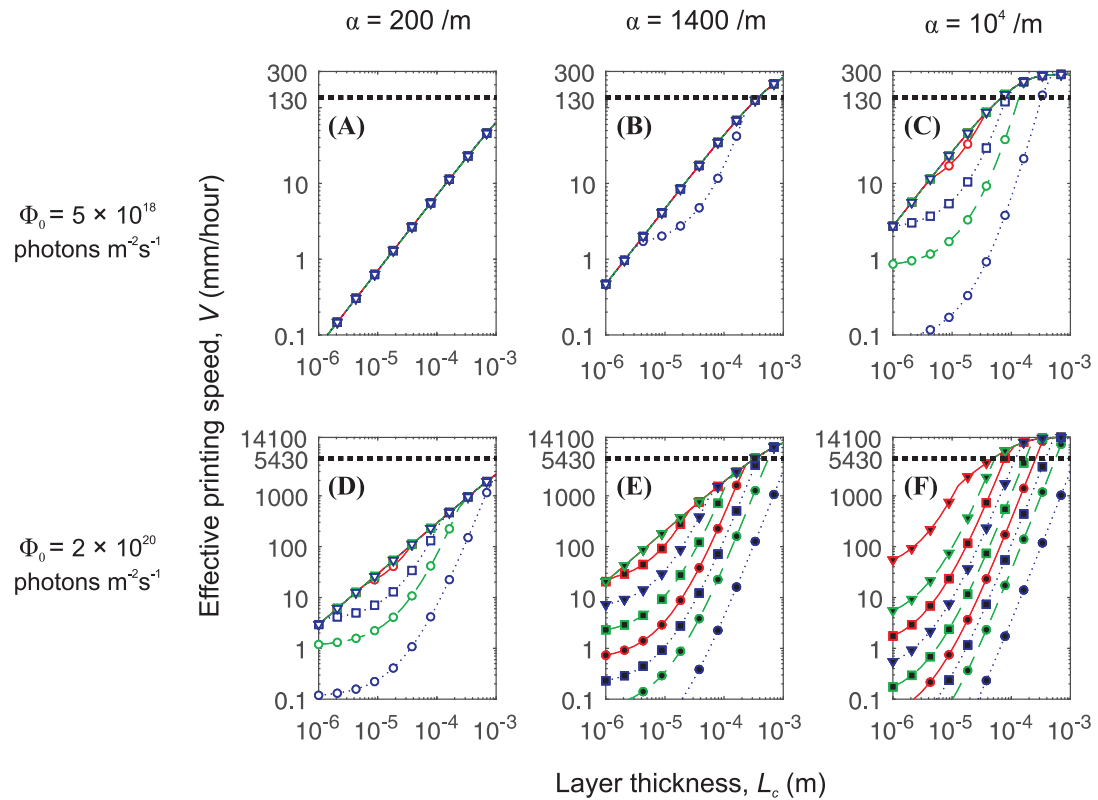


Fig. S16.

Speed comparison: CAL vs CLIP. Open symbols indicate that dead zone thickness, $h_d \geq 20 \mu\text{m}$. Black-shaded symbols indicate $h_d < 20 \mu\text{m}$. This set of curves holds for all values of H considered, although limitations of absolute of projector power may become relevant at large H .

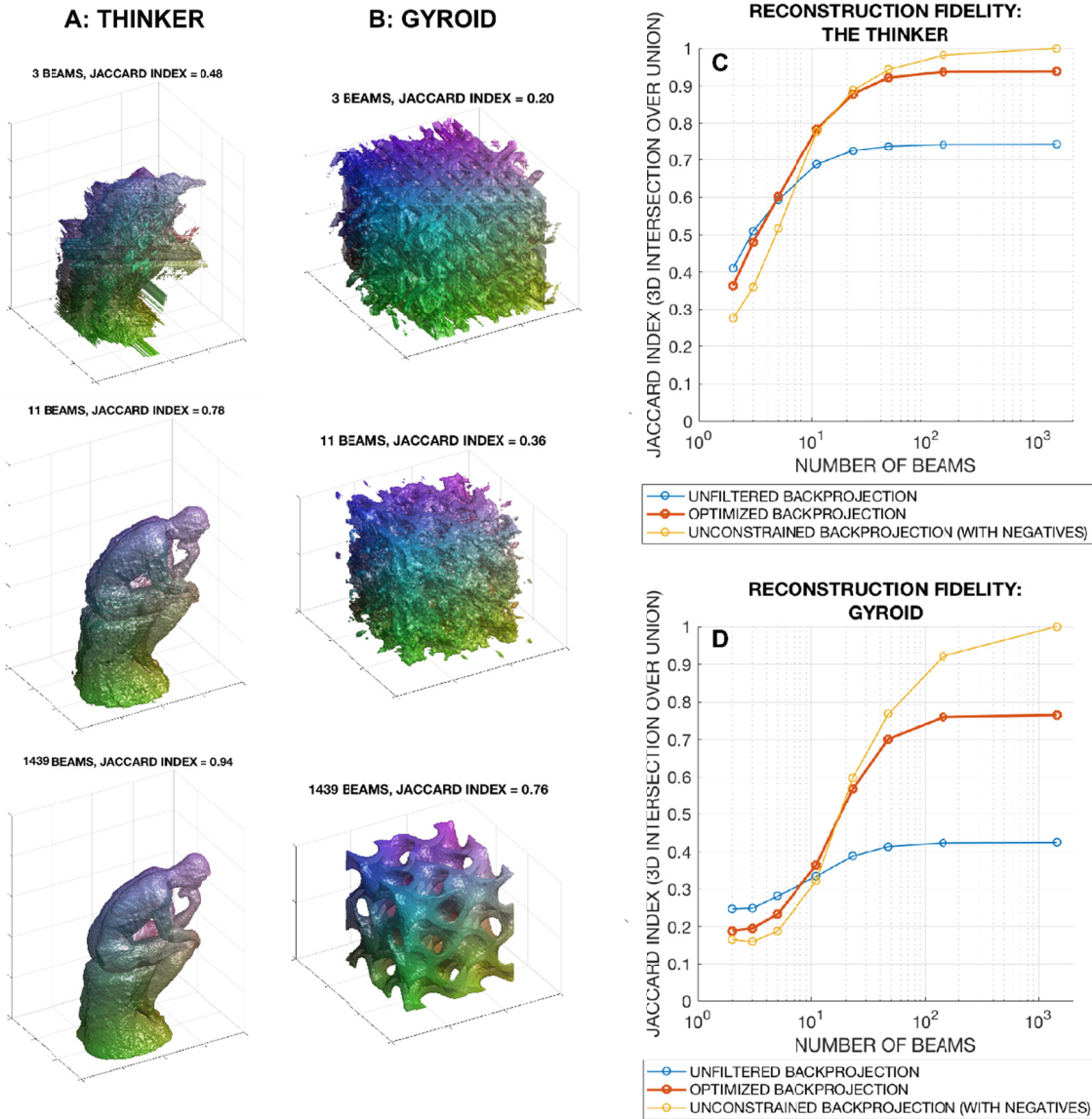


Fig. S17.

Dependence of reconstruction fidelity on angular sampling. (A): optimally thresholded reconstructions for the Thinker, using (top to bottom) 3, 11, and 1439 angular samples. (B): as (A), but for a gyroid. (C): Jaccard index (3D intersection over union) as a function of number of beams (*i.e.*, number of angular samples) for unfiltered, optimized and unconstrained backprojections for the Thinker. Optimized backprojections are used in CAL printing. (D): as (C), but for the gyroid geometry.

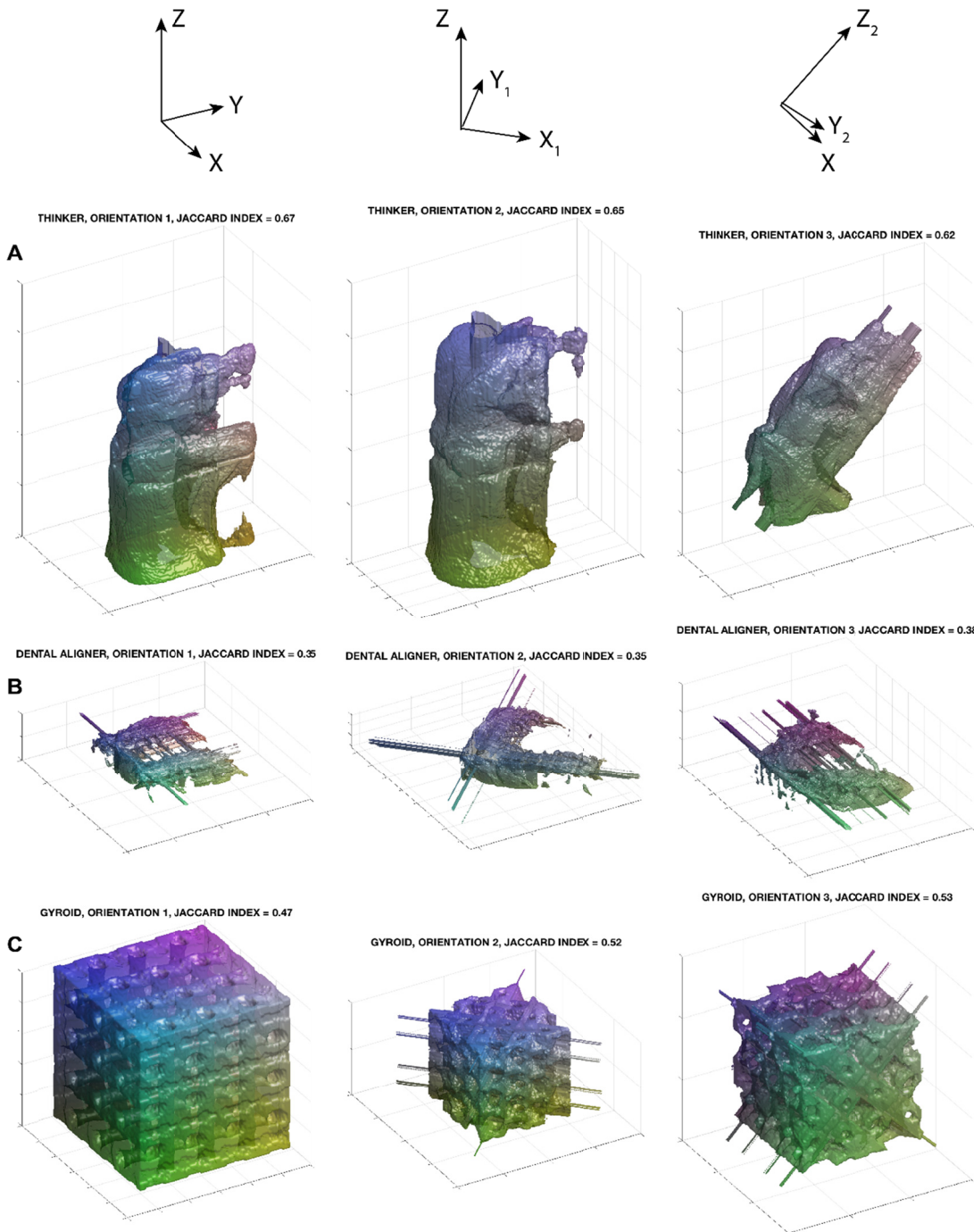


Fig. S18.

Reconstructions using three orthogonal directions (as in the method of (9)), with the orientations for the projections shown in the top row. (A): Thinker geometry; (B) dental aligner; (C) gyroid. Each geometry orientation is fixed as the projection directions change.

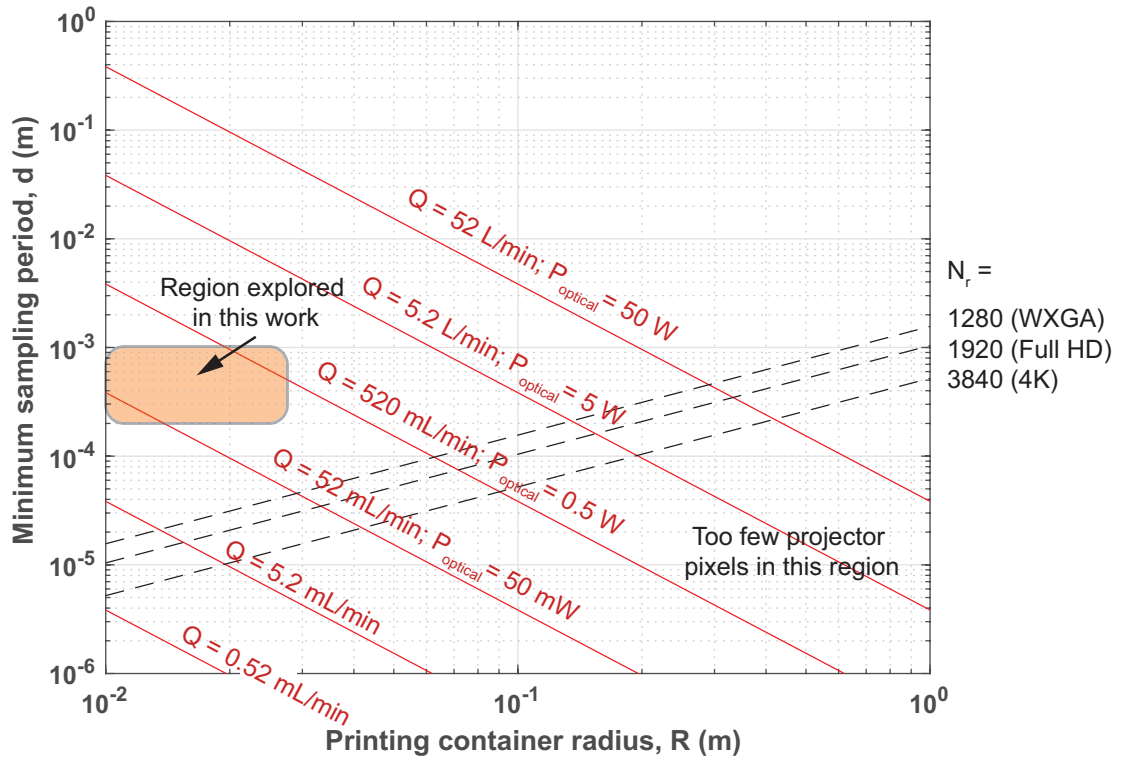


Fig. S19.

Relationship between minimum sampling period d (representing spatial resolution), container radius R , peak optical output power P_{optical} and volumetric print speed Q in CAL. In this chart, a curing dose of $D_{c0} = 4.9 \times 10^{22}$ photons/m³ (as found experimentally for our resin in Section S6), a projector refresh rate of $f_p = 25$ Hz, and illumination wavelength of 455 nm are assumed. These conditions are representative of the projector and resin used for many of the geometries shown in this paper; the region of geometries explored in the paper is indicated with a shaded box. Contours of illumination power P_{optical} and volumetric solidification rate Q are shown (red lines), as are constraints imposed by the number of pixels N_r across the width of projector hardware (black dashed lines).

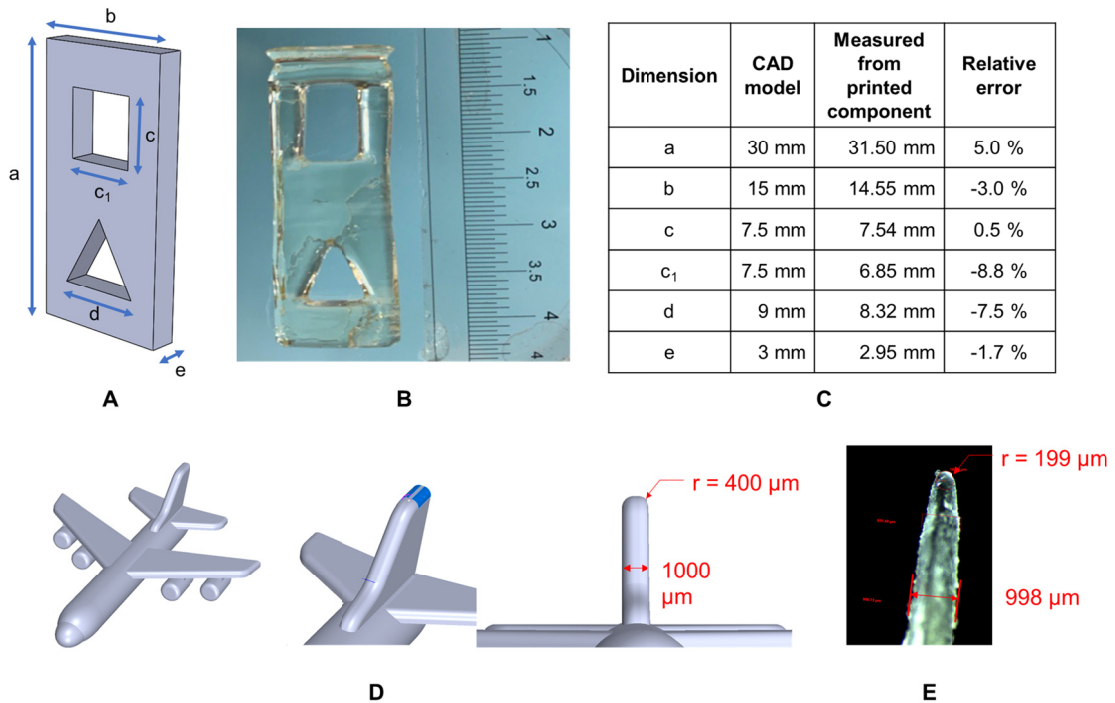


Fig. S20.

Dimensional comparison of CAL-printed objects with computer-aided design (CAD) drawings of the target objects. (A) CAD rendering of test artifact; (B) photograph of printed artifact (scale in cm); (C) summary of drawn and printed dimensions, and relative errors; (D) CAD renderings of airplane of Fig 2G with close-up of tail-fin tip; (E) Optical micrograph of printed tail-fin with key dimensions labeled.

Table S1.

Comparison of print speed models for PSL, CLIP and CAL.

	PSL	CLIP	CAL
Speed as governed purely by illumination time considerations, V_{ill}	$\left(\frac{\Phi_{0,PSL}}{D_c}\right) \frac{L}{L + h_d} e^{-1}$	$\frac{\Phi_{0,CLIP} e^{-\alpha_{CLIP} h_d}}{D_c} \left(1 - e^{-\alpha_{CLIP} L_c}\right)$	$\left(\frac{\Phi_{0,PSL}}{D_c}\right) e^{-1}$
Speed as governed purely by hydrodynamic considerations, V_{hyd}	$\frac{2p_{0,limit}L}{3\eta c_0^2} \left[\frac{1}{(h_d + L)^2} - \frac{1}{h_d^2} \right]^{-1}$	$-\frac{(h_d + L_c)^3}{3\eta c_0^2} p_{0,limit}$	No hydrodynamically imposed limit
Overall speed limit combining the illumination and hydrodynamic contributions, V	$V = (V_{ill}^{-1} + V_{hyd}^{-1})^{-1}$	$V = \min(V_{ill}, V_{hyd})$	$V = V_{ill}$

Table S2.

Parameters assumed for speed comparison of PSL, CLIP and CAL.

Parameter	Minimum considered	Maximum considered	Notes
Resin uncured viscosity, η	4 Pa.s \equiv 4000 cP		Mid-point between the measured viscosity, at low shear-rates, of the 3:1 BPAGDA/PEGDA resin used in our work (\sim 5000 cP), and the high end of the range reported for one typical resin used commercially in CLIP (1000–3000 cP, (43)).
Side-length of printing volume, H	1 cm	1 m	Chosen to span the system size in our work, current PSL/CLIP systems, and future, larger systems.
Absorption coefficient of resin, α	$2 \times 10^{-4} \mu\text{m}^{-1}$	$1 \times 10^{-2} \mu\text{m}^{-1}$	Consistent with values for the absorption coefficient arising from photoinitiator concentration only, α_{PI} , in Tumbleston (11). In this comparison we always assume that $\alpha = \alpha_{PI}$ (<i>i.e.</i> no dye) which will tend to favor PSL or CLIP in a speed comparison.
Maximum-magnitude hydrodynamic pressure, $p_{0,limit}$	-1 kPa	-1 MPa	This range encompasses plausible values for acceptable pressures. Since the typical yield strength of <i>fully cured</i> resins used in layer-by-layer printing is \sim 25 MPa (44), the acceptable tractions during printing (<i>i.e.</i> before the material has even reached the weaker ‘green’ state) can be expected to be far lower. Moreover, compliant hydrogels typically have elastic moduli \sim 1–10 kPa, so tractions would need to be well kept below this level to control distortions during printing of them.
Printed feature radius, a_0	1 mm	1 cm	This is a realistic feature-size range for industrially produced polymeric components.
Printed layer/slicing thickness, L or L_c	1 μm	1 mm	Encompassing the range considered by Tumbleston (11).
Photon flux of illumination, $\Phi_{0,PSL}$	$5 \times 10^{18} \text{ photons m}^{-2}\text{s}^{-1}$	$2 \times 10^{20} \text{ photons m}^{-2}\text{s}^{-1}$	$\Phi_{0,PSL} = \Phi_{0,CLIP} = \sqrt{2}\Phi_{0,CAL}$. Values chosen consistent with (11). At a central illumination wavelength of 455 nm, the highest flux in this range corresponds to \sim 87 W m $^{-2}$. Assuming an LED source in which 30% of photon flux is within a usable wavelength range, and a radiant efficiency of 40%, the LED input power for $H = 0.1$ m would be 7.25 W, corresponding to a projector power of \sim 700 lumens, well within commercial systems’ capabilities. Substantially larger printing volumes may require a scaling-up of projector power.

Table S3.

Comparison of predicted spin-up times for the present work and hypothetical scaled-up cases.

	Case A	Case B	Case C
	Present work	Scaled up print volume; standard video refresh rate	Scaled up print volume; micromirror switching limit
Dynamic viscosity of fluid, μ (Pa s)		5	
Density of fluid, ρ (kg m ⁻³)		1100	
Kinematic viscosity, $\nu = \mu/\rho$ (m ² s ⁻¹)		0.0045	
Container radius, R (m)	0.015	0.25	0.25
Frame rate of projector, f_p (Hz)	25	25	10,000
Angular velocity, Ω (rad/s)	0.26	0.26	105
Ekman spin-up time, t_{Ekman} (s)	0.62	10	0.51
Radial diffusion time, $t_{\text{Diffusion}}$ (s)	0.050	14	14
Rotational Reynolds number	0.013	3.6	1400

Movie S1. Thinker print

This video shows the Thinker' geometry of Fig. 1C–E. Projected images enter the vial from left to right across the video frames. The three-dimensional thinker object emerges within the rotating resin volume. Time since the onset of exposure as well as the rate of video speed up relative to real time are shown in the video frames at all times.

Movie S2. Thinker projection output frames

Computed two-dimensional patterned intensity images as output by the optical projection system during the ‘Thinker’ print. Frames are updated temporally and synced to the rotation rate of the photosensitive material volume.

Movie S3. Screwdriver overprint

Demonstration of the overprinting capability of CAL. A screwdriver handle is printed onto a mass-manufactured metal screwdriver blade.

Movie S4. Ball-in-a-cage print

This video shows the “ball-in-a-cage” geometry of Fig. 2E,F. As in Movie S1, projected images enter the vial from left to right across the video frames. Again, current exposure time and speed up rate are shown in the video frames at all times. A disconnected geometry emerges in the volume and is printed without sacrificial support structures.

Movie S5. Visualization of resin viscosity

This video shows two vials of BPAGDA/PEGDA resin mixture, one in the ratio 3:1 (left) and the other 7:1 (right). The vials are rotated by 90 degrees at room temperature and the subsequent flow under gravity is shown. The 7:1 mixture flows at a much slower rate, providing an intuitive sense of the properties of the materials in which CAL has been demonstrated.

References and Notes

1. E. MacDonald, R. Wicker, Multiprocess 3D printing for increasing component functionality. *Science* **353**, aaf2093 (2016). [doi:10.1126/science.aaf2093](https://doi.org/10.1126/science.aaf2093) [Medline](#)
2. X. Wang, S. Xu, S. Zhou, W. Xu, M. Leary, P. Choong, M. Qian, M. Brandt, Y. M. Xie, Topological design and additive manufacturing of porous metals for bone scaffolds and orthopaedic implants: A review. *Biomaterials* **83**, 127–141 (2016). [doi:10.1016/j.biomaterials.2016.01.012](https://doi.org/10.1016/j.biomaterials.2016.01.012) [Medline](#)
3. A. Bhargav, V. Sanjairaj, V. Rosa, L. W. Feng, J. Fuh Yh, Applications of additive manufacturing in dentistry: A review. *J. Biomed. Mater. Res. B* **106**, 2058–2064 (2018). [doi:10.1002/jbm.b.33961](https://doi.org/10.1002/jbm.b.33961) [Medline](#)
4. D. T. Nguyen, C. Meyers, T. D. Yee, N. A. Dudukovic, J. F. Destino, C. Zhu, E. B. Duoss, T. F. Baumann, T. Suratwala, J. E. Smay, R. Dylla-Spears, 3D-Printed Transparent Glass. *Adv. Mater.* **29**, 1701181 (2017). [doi:10.1002/adma.201701181](https://doi.org/10.1002/adma.201701181) [Medline](#)
5. H. Gong, B. P. Bickham, A. T. Woolley, G. P. Nordin, Custom 3D printer and resin for 18 μm \times 20 μm microfluidic flow channels. *Lab Chip* **17**, 2899–2909 (2017). [doi:10.1039/C7LC00644F](https://doi.org/10.1039/C7LC00644F) [Medline](#)
6. T. D. Ngo, A. Kashani, G. Imbalzano, K. T. Q. Nguyen, D. Hui, Additive manufacturing (3D printing): A review of materials, methods, applications and challenges. *Compos., Part B Eng.* **143**, 172–196 (2018). [doi:10.1016/j.compositesb.2018.02.012](https://doi.org/10.1016/j.compositesb.2018.02.012)
7. A. Gebhardt, J.-S. Hötter, *Additive Manufacturing: 3D Printing for Prototyping and Manufacturing* (Carl Hanser Verlag GmbH & Co. KG, München, 2016); www.hanser-elibrary.com/doi/book/10.3139/9781569905838.
8. E. Sachs, E. Wylonis, S. Allen, M. Cima, H. Guo, Production of Injection Molding Tooling With Conformal Cooling Channels Using the Three Dimensional Printing Process. *Polym. Eng. Sci.* **40**, 1232–1247 (2000). [doi:10.1002/pen.11251](https://doi.org/10.1002/pen.11251)
9. M. Shusteff, A. E. M. Browar, B. E. Kelly, J. Henriksson, T. H. Weisgraber, R. M. Panas, N. X. Fang, C. M. Spadaccini, One-step volumetric additive manufacturing of complex polymer structures. *Sci. Adv.* **3**, eaao5496 (2017). [doi:10.1126/sciadv.aao5496](https://doi.org/10.1126/sciadv.aao5496) [Medline](#)
10. C. W. Hull, Apparatus for production of three-dimensional objects by stereolithography, U.S. Patent 4,575,330 (1986).
11. J. R. Tumbleston, D. Shirvanyants, N. Ermoshkin, R. Janusziewicz, A. R. Johnson, D. Kelly, K. Chen, R. Pinschmidt, J. P. Rolland, A. Ermoshkin, E. T. Samulski, J. M. DeSimone, Additive manufacturing. Continuous liquid interface production of 3D objects. *Science* **347**, 1349–1352 (2015). [doi:10.1126/science.aaa2397](https://doi.org/10.1126/science.aaa2397) [Medline](#)
12. P. F. Jacobs, *Rapid Prototyping & Manufacturing: Fundamentals of StereoLithography* (Society of Manufacturing Engineers, Dearborn, MI, 1st edition, 1992).
13. G. N. Hounsfield, Method and apparatus for measuring x- or γ -radiation absorption or transmission at plural angles and analyzing the data, U.S. Patent 3,778,614 (1973).

14. J. Kastner, C. Heinzl, in *Integrated Imaging and Vision Techniques for Industrial Inspection* (Springer, London, 2015), *Advances in Computer Vision and Pattern Recognition*, pp. 227–250.
15. T. Bortfeld, J. Bürkelbach, R. Boesecke, W. Schlegel, Methods of image reconstruction from projections applied to conformation radiotherapy. *Phys. Med. Biol.* **35**, 1423–1434 (1990). [doi:10.1088/0031-9155/35/10/007](https://doi.org/10.1088/0031-9155/35/10/007) [Medline](#)
16. A. K. O'Brien, C. N. Bowman, Impact of oxygen on photopolymerization kinetics and polymer structure. *Macromolecules* **39**, 2501–2506 (2006). [doi:10.1021/ma051863l](https://doi.org/10.1021/ma051863l)
17. Materials and methods are available as supplementary materials.
18. S. S. Cutié, D. E. Henton, C. Powell, R. E. Reim, P. B. Smith, T. L. Staples, The effects of MEHQ on the polymerization of acrylic acid in the preparation of superabsorbent gels. *J. Appl. Polym. Sci.* **64**, 577–589 (1997). [doi:10.1002/\(SICI\)1097-4628\(19970418\)64:3<577:AID-APP14>3.0.CO;2-V](https://doi.org/10.1002/(SICI)1097-4628(19970418)64:3<577:AID-APP14>3.0.CO;2-V)
19. M. P. de Beer, H. L. van der Laan, M. A. Cole, R. J. Whelan, M. A. Burns, T. F. Scott, Rapid, continuous additive manufacturing by volumetric polymerization inhibition patterning. *Sci. Adv.* **5**, eaau8723 (2019). [doi:10.1126/sciadv.aau8723](https://doi.org/10.1126/sciadv.aau8723)
20. A. C. Kak, M. Slaney, *Principles of Computerized Tomographic Imaging* (Society of Industrial and Applied Mathematics, 2001).
21. G. N. Ramachandran, A. V. Lakshminarayanan, Three-dimensional reconstruction from radiographs and electron micrographs: Application of convolutions instead of Fourier transforms. *Proc. Natl. Acad. Sci. U.S.A.* **68**, 2236–2240 (1971). [doi:10.1073/pnas.68.9.2236](https://doi.org/10.1073/pnas.68.9.2236) [Medline](#)
22. J. Zhang, N. Pégard, J. Zhong, H. Adesnik, L. Waller, 3D computer-generated holography by non-convex optimization. *Optica* **4**, 1306–1313 (2017). [doi:10.1364/OPTICA.4.001306](https://doi.org/10.1364/OPTICA.4.001306)
23. R. Piestun, B. Spektor, J. Shamir, Wave fields in three dimensions: Analysis and Synthesis. *J. Opt. Soc. Am. A Opt. Image Sci. Vis.* **13**, 1837–1848 (1996). [doi:10.1364/JOSAA.13.001837](https://doi.org/10.1364/JOSAA.13.001837)
24. O. Tretiak, C. Metz, The Exponential Radon Transform. *SIAM J. Appl. Math.* **39**, 341–354 (1980). [doi:10.1137/0139029](https://doi.org/10.1137/0139029)
25. F. Natterer, Inversion of the attenuated Radon transform. *Inverse Probl.* **17**, 113–119 (2001). [doi:10.1088/0266-5611/17/1/309](https://doi.org/10.1088/0266-5611/17/1/309)
26. M. Ehrgott, Ç. Güler, H. W. Hamacher, L. Shao, Mathematical optimization in intensity modulated radiation therapy. *Ann. Oper. Res.* **175**, 309–365 (2010). [doi:10.1007/s10479-009-0659-4](https://doi.org/10.1007/s10479-009-0659-4)
27. S. V. Murphy, A. Atala, 3D bioprinting of tissues and organs. *Nat. Biotechnol.* **32**, 773–785 (2014). [doi:10.1038/nbt.2958](https://doi.org/10.1038/nbt.2958) [Medline](#)
28. J. W. Lee, P. X. Lan, B. Kim, G. Lim, D.-W. Cho, 3D scaffold fabrication with PPF/DEF using micro-stereolithography. *Microelectron. Eng.* **84**, 1702–1705 (2007). [doi:10.1016/j.mee.2007.01.267](https://doi.org/10.1016/j.mee.2007.01.267)

29. M. Hegde, V. Meenakshisundaram, N. Chartrain, S. Sekhar, D. Tafti, C. B. Williams, T. E. Long, 3D Printing All-Aromatic Polyimides using Mask-Projection Stereolithography: Processing the Nonprocessable. *Adv. Mater.* **29**, 1701240 (2017).
[doi:10.1002/adma.201701240](https://doi.org/10.1002/adma.201701240) [Medline](#)
30. A. S. Wu, W. Small Iv, T. M. Bryson, E. Cheng, T. R. Metz, S. E. Schulze, E. B. Duoss, T. S. Wilson, 3D Printed Silicones with Shape Memory. *Sci. Rep.* **7**, 4664 (2017).
[doi:10.1038/s41598-017-04663-z](https://doi.org/10.1038/s41598-017-04663-z) [Medline](#)
31. Printing rate modeling can be found in the supplementary materials, sections S18–S21.
32. K. S. Lim, B. S. Schon, N. V. Mekhileri, G. C. J. Brown, C. M. Chia, S. Prabakar, G. J. Hooper, T. B. F. Woodfield, New Visible-Light Photoinitiating System for Improved Print Fidelity in Gelatin-Based Bioinks. *ACS Biomater. Sci. Eng.* **2**, 1752–1762 (2016).
[doi:10.1021/acsbiomaterials.6b00149](https://doi.org/10.1021/acsbiomaterials.6b00149)
33. B. Kelly, I. Bhattacharya, M. Shusteff, H. Taylor, C. Spadaccini, Computed Axial Lithography (CAL) for Rapid Volumetric 3D Additive Manufacturing, presented at *Solid Freeform Fabrication* (2017); available at:
<http://sffsymposium.engr.utexas.edu/sites/default/files/2017/Manuscripts/ComputedAxialLithographyforRapidVolumetric3D.pdf> [accessed Aug. 16, 2018].
34. B. Kelly *et al.*, Computed Axial Lithography (CAL): Toward Single Step 3D Printing of Arbitrary Geometries. *arXiv:1705.05893 [cs]* (2017) (available at <http://arxiv.org/abs/1705.05893>).
35. D. M. Ebenstein, Nano-JKR force curve method overcomes challenges of surface detection and adhesion for nanoindentation of a compliant polymer in air and water. *J. Mater. Res.* **26**, 1026–1035 (2011). [doi:10.1557/jmr.2011.42](https://doi.org/10.1557/jmr.2011.42)
36. Carbon, Inc., Technical Data Sheet for Flexible Polyurethane (FPU) 3D Printer Material; available at www.carbon3d.com/materials/fpu-flexible-polyurethane/ [accessed Jan. 16, 2019].
37. N. Otsu, A Threshold Selection Method from Gray-Level Histograms. *IEEE Trans. Syst. Man Cybern.* **9**, 62–66 (1979). [doi:10.1109/TSMC.1979.4310076](https://doi.org/10.1109/TSMC.1979.4310076)
38. P. Kuchment, Generalized Transforms of Radon Type and their Application, in *The Radon Transform, Inverse Problems, and Tomography*, vol. 63 of *Proceedings of Symposia in Applied Mathematics*, eds. G. Ólafsson, E. Quinto, American Mathematical Society (2006). DOI: [10.1090/psapm/063/2208237](https://doi.org/10.1090/psapm/063/2208237)
39. X. Zhang, X. N. Jiang, C. Sun, Micro-stereolithography of polymeric and ceramic microstructures. *Sens. Actuators A* **77**, 149–156 (1999). [doi:10.1016/S0924-4247\(99\)00189-2](https://doi.org/10.1016/S0924-4247(99)00189-2)
40. C. Sun, N. Fang, D. M. Wu, X. Zhang, Projection micro-stereolithography using digital micro-mirror dynamic mask. *Sens. Actuators A* **121**, 113–120 (2005).
[doi:10.1016/j.sna.2004.12.011](https://doi.org/10.1016/j.sna.2004.12.011)
41. H. M. Laun, M. Rady, O. Hassager, Analytical solutions for squeeze flow with partial wall slip. *J. Non-Newt. Fluid Mech.* **81**, 1–15 (1999). [doi:10.1016/S0377-0257\(98\)00083-4](https://doi.org/10.1016/S0377-0257(98)00083-4)

42. X. Zheng, H. Lee, T. H. Weisgraber, M. Shusteff, J. DeOtte, E. B. Duoss, J. D. Kuntz, M. M. Biener, Q. Ge, J. A. Jackson, S. O. Kucheyev, N. X. Fang, C. M. Spadaccini, Ultralight, ultrastiff mechanical metamaterials. *Science* **344**, 1373–1377 (2014).
[doi:10.1126/science.1252291](https://doi.org/10.1126/science.1252291) [Medline](#)
43. Carbon, Inc., Safety Data Sheet for UMA90 resin; available at: www.tth.com/wp-content/uploads/103367-UMA-90-US-SDS.pdf [accessed Aug. 14, 2018].
44. Carbon, Inc., Technical Data Sheet for UMA90 resin; available at:
https://s3.amazonaws.com/carbon-static-assets/downloads/resin_data_sheets/UMA90_TDS.pdf [accessed Aug. 15, 2018].
45. S. Yuan, F. Liu, J. He, Preparation and Characterization of Low Polymerization Shrinkage and Bis-GMA-Free Dental Resin System. *Adv. Polym. Technol.* **34**, 21503 (2015).
[doi:10.1002/adv.21503](https://doi.org/10.1002/adv.21503)
46. H. P. Greenspan, L. N. Howard, On a time-dependent motion of a rotating fluid. *J. Fluid Mech.* **17**, 385–404 (1963). [doi:10.1017/S0022112063001415](https://doi.org/10.1017/S0022112063001415)
47. W. B. Watkins, R. G. Hussey, Spin-up from rest in a cylinder. *Phys. Fluids* **20**, 1596–1604 (1977). [doi:10.1063/1.861781](https://doi.org/10.1063/1.861781)
48. J. Sharpe, U. Ahlgren, P. Perry, B. Hill, A. Ross, J. Hecksher-Sørensen, R. Baldock, D. Davidson, Optical projection tomography as a tool for 3D microscopy and gene expression studies. *Science* **296**, 541–545 (2002). [doi:10.1126/science.1068206](https://doi.org/10.1126/science.1068206) [Medline](#)
49. H. Zollinger, *Color Chemistry: Syntheses, Properties, and Applications of Organic Dyes and Pigments* (John Wiley & Sons, 2003).
50. Luminus Devices, Inc, Luminus CBT-39 LED product datasheet; available at
https://download.luminus.com/datasheets/Luminus_CBT-39-UV_Datasheet.pdf [accessed Jan. 16, 2019].